Journal of Materials Chemistry A

Structural Complexity in a Highly Reversible "Anion-Redox" Cathode

Journal:	*Journal of Materials Chemistry A*
Manuscript ID	TA-ART-02-2025-001450.R1
Article Type:	Paper
Date Submitted by the Author:	18-Apr-2025
Complete List of Authors:	Bassey, Euan; University of California Santa Barbara, Materials Lawrence, Erick; University of California Santa Barbara, Materials Korjus, Ove; Institut Laue-Langevin Suard, E.; Institut Laue-Langevin, ; Institut Laue Langevin Van der Ven, Anton; University of California Santa Barbara Clément, Raphaële; University of California, Santa Barbara, Materials Research Laboratory

Structural Complexity in a Highly Reversible "Anion-Redox" Cathode

Euan N. Bassey,[†,‡] Erick A. Lawrence,[†,‡] Ove Korjus,[¶] Emmanuelle Suard,[¶] Anton Van der Ven,[*,†] and Raphaële J. Clément[*,†,‡]

†*Materials Department, University of California Santa Barbara*
‡*Materials Research Laboratory, University of California Santa Barbara*
¶*Institut Laue Langevin*

E-mail: avdv@ucsb.edu; rclement@ucsb.edu

Abstract

Li-rich cathodes with an O2-type layer stacking offer high gravimetric capacities and fast charge-discharge rates, and are structurally more stable with respect to transition metal migration than O3-type Li-rich cathodes. However, the nature and reversibility of their charge-discharge processes remain poorly understood, in part because these materials can only be obtained through soft chemistry routes. This work provides a new structural model for a recently-reported O2-type cathode with nominal composition $Li_{1.1}Al_{0.04}Mn_{0.65}Ni_{0.21}O_2$ and excellent structural and potential stability. Our new model hints at the impact of short-range cation ordering and phase separation on the electrochemical performance. Neutron and X-ray diffraction indicate that the as-synthesized compound comprises two crystallographically distinct phases—a Li_2MnO_3 component and a Li-poor ($Li_{0.78}Al_{0.02}Mn_{0.67}Ni_{0.31}O_2$) component—most likely stacked epitaxially along the *c*-axis. ^{7}Li, ^{17}O and ^{27}Al solid-state NMR measurements further reveal a tendency towards honeycomb ordering on the transition metal sublattice—long-range ordering in Li_2MnO_3 and partial, short-range ordering in $Li_{0.78}Al_{0.02}Mn_{0.67}Ni_{0.31}O_2$—and highlight the presence of dilithium environments within the transition metal layer in Li_2MnO_3, with important consequences on structural stability during electrochemical cycling.

Introduction

High capacity cathodes are anticipated to be critical for the wider uptake of rechargeable batteries in electronic devices, electric and hybrid-electric vehicles, and as grid-scale load levelers to renewable energy sources. In particular, intercalation compounds that exhibit anion redox have garnered significant attention in recent years as high capacity cathodes for Li- and Na-ion batteries.[1–8] Here, we define anion redox as anything beyond conventional transition metal (*TM*) redox, and involving electronic states that the anion (typically oxide, O^{2-}) contributes to significantly.[7,9–18] In layered Li-ion oxide cathodes, where the Li^+ ions occupy two-dimensional galleries between layers of edge-sharing *TM* oxide octahedra, anion redox is commonly achieved by substituting *TM* cations by Li, resulting in a "Li-rich" composition.[2,3,7,19–21]

Despite their promise, anion redox oxide cathodes invariably suffer from a large potential hysteresis (where the difference between the charge and discharge potentials far exceeds the polarization in conventional *TM* redox-only cathodes), capacity loss, and potential fade.[7,22] While the precise mechanism of anion redox remains under debate, and depends sensitively on the composition and

local structure (short-range ordering) of the cathode, it is widely acknowledged that potential hysteresis, capacity loss and potential fade, are all associated with structural alterations during cycling.[8,14–17,23–27] Hence, in understanding the structural evolution of anion redox cathodes during cycling, it is vital to have a clear picture of the long- and short-range structure of the pristine material.

Most studies of anion redox compounds have focused on Li-rich layered oxide cathodes with an O3 structure. In such cathodes, interlayer *TM* migration involves a *TM* cation dropping from an octahedral site in the *TM* layer into an adjacent tetrahedral site in the Li layer face-sharing with three vacant octahedral Li sites (generated on delithiation or charge), as shown in Figure 1(a). Subsequent in-plane migration of this *TM* species to a neighboring octahedral site is associated with a relatively low energy penalty, since the migrated *TM* does not share faces with nearby *TM* cations in the layers above and below (see Figure 1(a)). Consequently, the *TM* cation can move away from the vacancy created in the *TM* layer without incurring a large energy penalty, and this in turn irreversibly changes the structure.

One strategy to mitigate long-range *TM* migration is to move away from an O3 layer stacking sequence. For example, for an O2 layer stacking, *TM* cation migration from the *TM* layer into either a tetrahedral site or an octahedral site in the partially-delithiated Li layer may take place, but subsequent migration within the Li layer is precluded by the large Coulombic repulsion with *TM* sites that share a face with the Li layer tetrahedral or octahedral sites [Figure 1(b)].[28] Hence, irreversible structural transformations *via TM* migration are suppressed. In this regard, the O2 structural family offers a chance to realize anion redox in Li-rich layered oxides without significant rearrangements of the TM sublattice.[29] We note that O2 Li-ion cathodes cannot be synthesized by conventional solid-state reactions, but instead are prepared *via* ion exchange, typically starting from a P2 Na-ion cathode.[30] Consequently, O2 cathodes have complex, multi-component structures, containing structural motifs inherited from the P2 precursor (*e.g.*, cation ordering) as well as additional structural elements (*e.g.*, stacking faults) that are introduced during ion exchange.

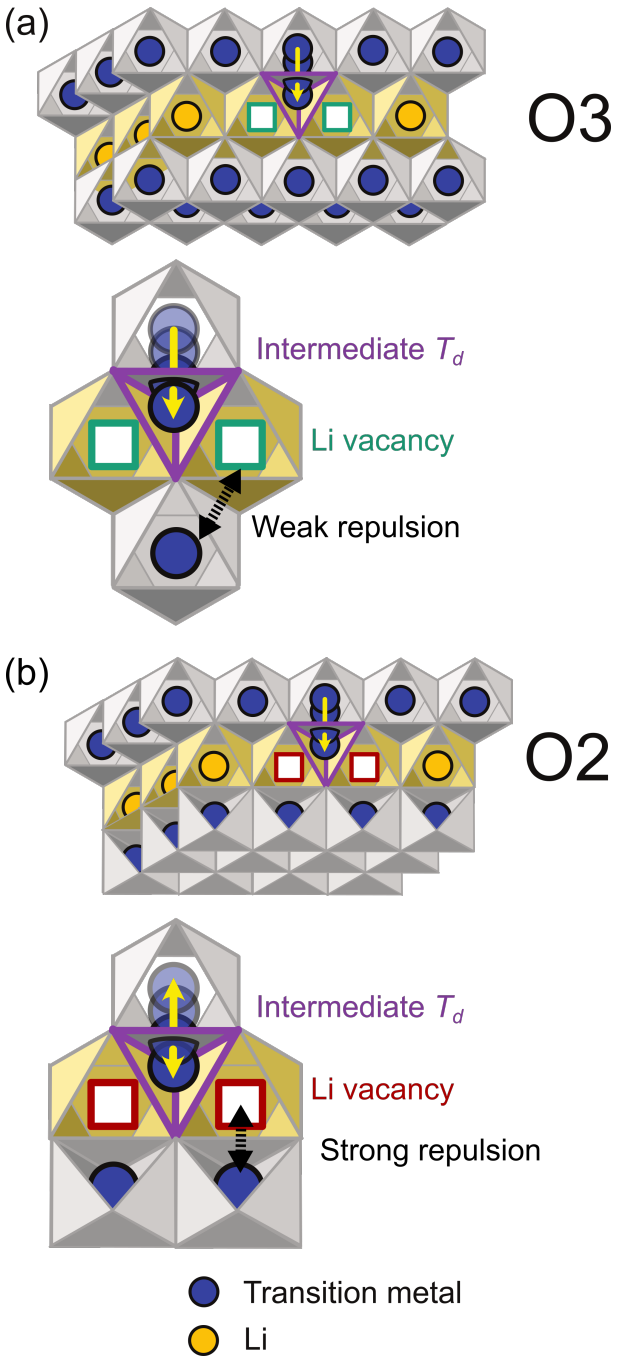

Figure 1: Structures of O2 and O3 layered cathodes. In **(a)**, the interlayer *TM* migration process is shown, with the tetrahedral intermediate highlighted in purple, alongside the octahedral Li vacancies (green squares) that the *TM* can readily hop into. The *TM* migration process for O2 cathodes is depicted in **(b)**, the tetrahedral intermediate again in purple; the high-energy vacant octahedral Li sites that share faces with the nearby *TM* sites (red squares) are high in energy.

Leveraging the structural stability imparted by

the O2 layered structure, several recent studies have investigated anion redox activity in this class of cathodes.[29,31] Luo *et al.*[32] reported on a novel O2 cathode with nominal composition $Li_{1.1}Al_{0.04}Mn_{0.65}Ni_{0.21}O_2$ (henceforth LAMNO) and exceptional electrochemical performance, including almost no potential fade over 100 cycles. The structure was described as comprising two phases: an O2-stacked Li_2MnO_3 structure and an O2 Li-stoichiometric material containing Mn, Ni and Al on the *TM* sublattice (whose composition was not stated), based on previous reports and qualitative comparisons of calculated and observed X-ray diffraction patterns. Furthermore, the favorable performance of LAMNO was attributed to the presence of anti-site Ni defects hypothesized to prevent *TM* migration. The justification for these defects came from transmission electron microscopy. While the study of Luo *et al.* showed that LAMNO is a very promising anion redox cathode material, many questions remain about the local structure and its impact on the electrochemical behavior of the material.

Here, we revisit the structure of the pristine LAMNO cathode. We use powder X-ray diffraction (PXRD) and powder neutron diffraction (PND) to evaluate the long-range structure, and identify the coexistence of two phases, namely O2-Li_2MnO_3 and a Li-poor phase ($Li_{0.78}[Al_{0.02}Mn_{0.67}Ni_{0.31}]O_2$), consistent with the findings from Luo *et al.*[32] and analogous to the composite structure reported for some Li-rich O3 cathodes.[3,33,34] Our neutron diffraction results provide no evidence for the presence of *TM* cations in the interlayer space, contrary to the previous report by Luo *et al.*[32] Furthermore, a computational investigation fails to identify thermodynamically stable configurations with Ni, Mn and/or Al in the interlayer of LAMNO. Results from multinuclear (^{7}Li, ^{17}O and ^{27}Al) solid-state nuclear magnetic resonance (NMR) spectroscopy reveal the presence of a local ordering of the *TM* cations in both the O2-Li_2MnO_3 and Li-poor phases, and highlight the presence of "dilithium" environments in the *TM* layer of Li_2MnO_3, whereby Li ion pairs are surrounded by Mn^{4+} ions. Finally, we suggest a connection between these dilithium environments and the electrochemical performance observed for this material.

Methods

Synthesis. The method used to synthesize LAMNO was broadly similar to the previously-reported route (see Supporting Information, SI, for more details).[32] Briefly, LAMNO was prepared from a P2 layered sodium analogue, $Na_{0.67}Al_{0.02}Mn_{0.67}Ni_{0.23}O_2$ (henceforth NAMNO), using chemical ion exchange. NAMNO was synthesized in 1–2 g batches *via* a high-temperature solid-state reaction (10 hr at 780°C under air, then cooled naturally to room temperature) starting from Na_2CO_3, Al_2O_3, Li_2CO_3 and $Mn_{0.75}Ni_{0.25}CO_3$ (the latter synthesized *via* co-precipitation of $NiSO_4 \cdot 6H_2O$ and $MnSO_4 \cdot H_2O$ in the presence of Na_2CO_3). To synthesize LAMNO, the NAMNO powder was added to a molten salt (0.12 LiCl and 0.88 $LiNO_3$ at 280°C) and reacted for approximately 6 hours before quenching in water, filtering and drying the resulting powder under dynamic vacuum at 180°C for 12 hr. Both materials were stored in an Ar-filled glovebox (MBraun, H_2O, O_2 < 5 ppm).

Electrochemistry. All electrochemical measurements were conducted using 2032 stainless-steel coin cells and a galvanostat/potentiostat (BioLogic) with EC laboratory software. Each LAMNO||Li half-cell comprised a cathode (6 mm diameter), a glass fibre separator (GF/B, Whatman, 16 mm diameter) soaked with 150μL of electrolyte (1.0 M $LiPF_6$ in a 1:1:1 v/v mixture of ethylene carbonate diethyl carbonate and dimethyl carbonate), and a Li metal disc (13 mm diameter). The cells were cycled at a rate of 10 mA g^{-1}, corresponding to approximately *C*/20, for a theoretical *C*-rate relative to that of the pristine material. This *C*-rate was calculated by assuming that the Li content, *x*, in the pristine material is 0.93 (based on compositional analysis of as-synthesized LAMNO), and that *x* can vary between 0 and 1 on cycling. The experimentally determined values of *x* used for plotting were computed from the time elapsed and current applied assuming no parasitic reactions.

Powder X-ray Diffraction. Laboratory powder X-ray diffraction (PXRD) patterns of NAMNO were recorded using a PANalytical Empyrean diffractometer (Cu $K\eta$ radiation, λ = 1.541 Å). The sample was sealed in an air-tight sample holder using polyimide (Kapton) film and patterns were acquired over the range 2θ =

5–90°, with a step size of 0.02°and a scanning speed of $0.02°s^{-1}$. For synchrotron diffraction data on LAMNO, powder samples of pristine LAMNO were sealed in a borosilicate capillary (outer diameter 0.5 mm). Powder X-ray diffraction patterns were acquired on beamline I11 at the Diamond Light source.[35,36] The pattern(s) were collected with an exposure time of 1 minute using a position-sensitive detector (PSD, Methen2; X-ray wavelength = 0.824297 Å) over the range 2θ = 2.0 - 65°. All Rietveld[37,38] refinements were carried out using the TOPAS Academic 7.0 structure refinement software package.[39,40]

Powder Neutron Diffraction. Powder neutron diffraction measurements were carried out at the Institut Laue-Langevin using the D2B instrument.[41] A powder sample of pristine LAMNO was loaded into a thin-walled vanadium canister (5 mm diameter). The background was fit using a 12-term Chebyshev polynomial, and the lattice parameters were refined alongside the site occupancies for Li, Al, Mn and Ni.

Inductively Coupled Plasma. Inductively coupled plasma (ICP) measurements were carried out using an Agilent 5900 ICP optical emission spectrometer (OES). A powder sample of LAMNO (approximately 10 mg) was first digested in aqua regia (HNO_3:HCl 4:1 v/v, 5 mL) overnight, and an aliquot (0.5 mL) diluted in 3% v/v HNO_3 (7.5 mL). Standards of Mn, Ni, Al and Li (1000 ppm each) were purchased from Texas Scientific Products and subsequently diluted in 3% v/v HNO_3 to concentrations of 100, 50, 25, 10, 1 and 0.1 ppm. The following elemental emission lines were selected from the spectra: 231.604 nm (Ni), 260.568 (Mn), 396.152 (Al) and 610.365 nm (Li). The standards were then measured and calibration curves of intensity versus concentration built to within a linear regression r^2 limit of 0.999. The stoichiometry of the sample was determined to be $Li_{1.00}Al_{0.04}Mn_{0.67}Ni_{0.23}O_2$.

Scanning Electron Microscopy. Scanning Electron Microscopy (SEM) images were acquired with a Thermo Scientific Apreo S SEM instrument operating at an acceleration potential of 10 kV and current of 0.2 nA.

Nuclear Magnetic Resonance Spectroscopy. LAMNO and NAMNO powder samples were packed into 1.3 mm diameter ZrO_2 magic angle spinning (MAS) rotors in an Ar-filled glovebox; no rotor spent longer than 10 minutes outside of the glovebox before being inserted into the magnet under a protective atmosphere of flushing nitrogen gas. NMR spectra were referenced to 1.0 M aqueous LiCl (^{7}Li, 0 ppm), H_2O (^{17}O, 0 ppm) or $Al(NO_3)_3$ (^{27}Al, 0 ppm). ^{7}Li NMR spectra were recorded on a Bruker AVANCE (2.35 T) using a home-built 1.3 mm MAS probe, an MAS frequency of 60 kHz, and a $\pi/2$ pulse length of 1.75 μs. ^{17}O and ^{27}Al NMR spectra were recorded on a Bruker AVANCE III (11.7 T) using a Bruker 1.3 mm MAS probe, an MAS frequency of 60 kHz, and effective $\pi/2$ pulse lengths of 0.75 μs and 0.31 μs, respectively, which corresponds to $\frac{\pi}{6}$, to obtain quantitative spectra in the presence of strong quadrupolar interactions between the nuclei of interest and the local electric field gradient.[42]

Rotor-synchronized Hahn-echo pulse sequences were used throughout; in the case of ^{27}Al and ^{17}O, spectra were acquired at different receiver frequency offsets to record individual slices in a variable-offset cumulative spectrum (VOCS). The recycle delay (100 ms for ^{7}Li; 5 ms for ^{17}O and ^{27}Al) was set such that the bulk, paramagnetically shifted signal was recorded quantitatively, while the diamagnetic signal (due to small quantities of amorphous impurities at the surface of particles) was suppressed. In the case of ^{7}Li, we also acquired a spectrum with a longer recycle delay, 10 s, quantitative for the diamagnetic signal. Projection magic angle turning phase-adjusted sideband suppression (pj-MATPASS) experiments were also recorded to separate the isotropic resonances from the overlapping spinning sideband manifold.[43] Relaxation times, including spin-lattice (T_1) and spin-spin (T_2), were recorded using saturation-recovery and pseudo two-dimensional Hahn-echo experiments, respectively.

First-Principles Calculations of NMR Hyperfine and Quadrupolar Shifts. Three structural models were used to determine the shifts of ^{7}Li, ^{17}O and ^{27}Al in LAMNO: O2-Li_2MnO_3 (cell composition: $Li_{32}Mn_{16}O_{48}$; $a = b \approx 9.7$ Å, $c \approx 9.5$ Å), O2-$Li[Ni_{1/3}Mn_{2/3}]O_2$ (cell composition: $Li_{24}Ni_8Mn_{16}O_{48}$, $a \approx 9.9$ Å, $b \approx 10.0$ Å, $c \approx 9.8$ Å) and O2-$Li_{2/3}[Ni_{1/3}Mn_{2/3}]O_2$ (cell composition: $Li_{16}Ni_8Mn_{16}O_{48}$, $a = b \approx 9.9$ Å, $c \approx 9.8$ Å). These cells correspond to ($2 \times 2 \times 2$) supercells of the primitive structures ($Li_4Mn_2O_6$; $Li_3Ni_1Mn_2O_6$; $Li_2Ni_1Mn_2O_6$), chosen to capture all interlayer and intralayer interactions between the nuclides of interest (Li, Al and O) and neighboring paramagnetic transition metal centers. For ^{27}Al NMR shift calculations, cells were prepared starting from the O2-$Li[Ni_{1/3}Mn_{2/3}]O_2$ structure and partially substituting Ni or Mn species by Al to reach a composition of $Li_{24}Al_1Ni_7Mn_{16}O_{48}$ or $Li_{24}Al_1Ni_8Mn_{15}O_{48}$.

^{7}Li, ^{17}O and ^{27}Al paramagnetic (or hyperfine) and quadrupolar shifts for each site in the structures of interest were calculated using methods described

previously.[44–47] All calculations were performed on ferromagnetically-aligned cells, unless stated otherwise. Shifts were scaled from 0 K to room temperature using experimental magnetic susceptibility data [Supplemental Note 1].

An initial geometry optimization was performed using the VASP code,[48–50] employing the projector-augmented wave method.[51,52] These calculations employed the SCAN *meta*-GGA exchange-correlation functional,[53–55] and a plane-wave cutoff energy set to 520 eV. All structural optimizations were performed with a reciprocal space discretization of 0.04 $Å^{-1}$ without assuming any symmetry.[56] All electronic structures were converged to 10^{-5} eV for energies, while forces on atoms were converged to 0.02 eV $Å^{-1}$.

Periodic spin-polarized hybrid density functional theory (DFT) calculations of the hyperfine and quadrupolar-induced shifts were performed in CRYSTAL.[57–59] Hyperfine parameters were calculated with a modified B3LYP[60,61] hybrid functional containing 20 and 35% Hartree-Fock exchange, referred to as Hyb20 and Hyb35, respectively. These weights were chosen based on the success of these functionals in calculating Fermi contact shifts and hyperfine tensors, and magnetic properties of *TM* compounds and have been previously reported to provide upper and lower bounds on experimental shifts.[44–46] The calculations employed extended basis sets, taken from the Ahlrichs set for metal ions[62] and the IGLO-III basis set for O.[63] Additional information, including the number of Gaussian primitives and contraction scheme used for each basis set, alongside details of convergence criteria used, are provided in the SI.

First-Principles Calculations of Anti-Site Formation Energies and *TM* Ordering. Structures containing different concentrations of Mn, Ni and Al anti-sites, and different *TM* configurations, were enumerated using the CASM software package,[64] and their formation energies were computed with VASP using the same computational parameters as described above. To sample compositions and anti-site defect concentrations that are consistent with previous work,[32] large supercells of O2-Li_2MnO_3 and O2-$Li_{2/3}[Ni_{1/3}Mn_{2/3}]O_2$ (typically at least three times larger in volume than the primitive cell containing four *TM* sites) were required. Given the large number of possible configurations in such large supercells, a thorough sampling of all structures was computationally intractable and a more pragmatic approach was used instead, where at least 200 configurations were sampled randomly for each composition of interest.

Results

Analysis of the Na-containing precursor and pristine O2 cathode

We begin with a brief analysis of the Na-containing precursor, NAMNO, since the structure of this P2 cathode dictates the structure of the LAMNO cathode of interest. The Rietveld refinement of the powder X-ray diffraction (PXRD) pattern collected on as-synthesized NAMNO and corresponding structural model are shown in Figures S1 and S2, respectively. The refinement parameters are listed in Table S1. A two-phase model was required to accurately fit the data. The two phases were: (1) a high symmetry ($P6_3mmc$) P2 phase with composition $Na_{0.70}Mn_{0.67}Ni_{0.31}Al_{0.02}O_2$, accounting for approximately 70 wt.% of the sample, and (2) a lower-symmetry ($Cmc2_1$) phase with composition $Na_{0.82}Mn_{0.67}Li_{0.33}O_2$, making up for approximately 30 wt.% of the sample. In the second phase, Li and Mn preferentially occupy different *TM* layer sites, and some anti-site disorder is also present [Table S1]. The small peak observed at about $Q = 1.4Å^{-1}$ indicates some amount of honeycomb ordering within the *TM* layers. The low intensity of the $Q = 1.4Å^{-1}$ peak likely arises from the presence of stacking faults and anti-site disorder,[65–67] as discussed in more detail later. The compositions of the two Na-containing phases were determined from refinement of the X-ray diffraction data, and our results do not indicate any Ni, Mn or Al in the Na layers.

We hereafter analyze the target LAMNO cathode in detail. First, the composition of the cathode was determined using inductively coupled plasma (ICP), which provides the bulk sample composition, and ^{7}Li solid-state nuclear magnetic resonance (NMR) spectroscopy, which provides quantitative information about the fraction of Li in the cathode and in possible impurity phases, whether these are crystalline or amorphous. The sample composition obtained

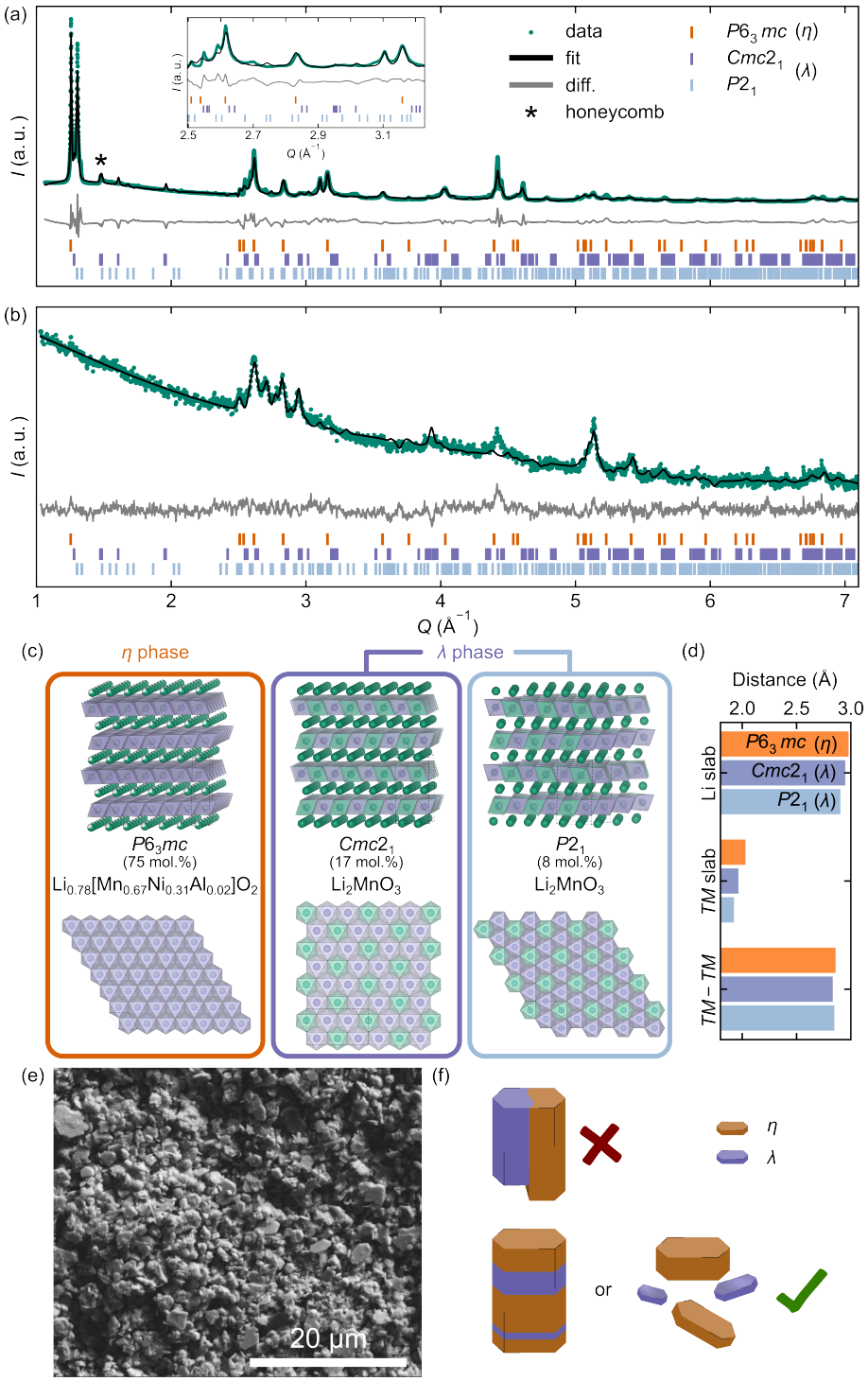

Figure 2: Simultaneous Rietveld refinements of the **(a)** Synchrotron powder x-ray diffraction (PXRD) ($R_{\text{w.p.}} = 10.6\%$) and **(b)** powder neutron diffraction (PND) patterns ($R_{\text{w.p.}} = 8.9\%$) recorded at room temperature on pristine LAMNO. Inset shows the region of the X-ray diffraction pattern, from $Q = 2.5\text{Å}^{-1} - 3.2\text{Å}^{-1}$, corresponding to the broader (hkl)-type reflections that are broader and more challenging to fit. In **(c)**, the refined structures are shown, with both views of the overall cell and of the *TM* layers. The Li and TM slab thicknesses of each phase, as well as the intralayer *TM*–*TM* distances, are shown in **(d)** for each structure. In **(e)**, a scanning electron microscopy (SEM) image of the pristine material is shown, acquired at 3500× magnification. The possible distribution of the two phases within and across particles is shown in **(f)**.

from ICP is $Li_{1.00}Al_{0.04}Mn_{0.67}Ni_{0.23}O_2$, while ^{7}Li NMR indicates that Li-containing diamagnetic

impurity phases (e.g., Li_2CO_3, Li_2O, LiOH), giving rise to the sharp resonance at approximately 0 ppm in the quantitative Hahn-echo spectrum in Figure S3, make up for approximately 7% of the total Li in the sample. The ^{7}Li NMR results are presented and discussed in more detail later. Based on the ICP and ^{7}Li NMR quantification, the composition of the electrochemically active component of the LAMNO cathode comes out as $Li_{0.93}Al_{0.04}Mn_{0.67}Ni_{0.23}O_2$.

The PXRD and powder neutron diffraction (PND) patterns obtained for pristine LAMNO were refined simultaneously using three previously-reported O2 structural models [Figures 2(a) and (b)]:[32,68] a high-symmetry hexagonal ($P6_3mc$) phase, in which the *TM* sublattice comprises Mn (67%), Ni (31%) and Al (2%), and two phases containing Li and Mn in a *ca.* 1:2 ratio in the *TM* layers (space groups $Cmc2_1$ and $P2_1$), that are approximately honeycomb ordered (*i.e.*, Li_2MnO_3-like). We note that the intensity of the neutron diffraction patterns are much lower than expected, owing to a low amount of sample in the canister due to the difficulty in generating large batches of the ion-exchanged material. The atomic structures of these three phases are depicted in Figure 2(c). We henceforth refer to the high-symmetry, Li-poor, Ni/Mn/Al-containing phase as the η phase, and to the two lower-symmetry, Li-rich, Mn-only phases as the λ phases [2(c)].

The (00l) and (hk0) reflections from all phases of LAMNO are, in general, sharp, while the (hkl) reflections with non-zero Miller indices are broad, indicative of stacking faults and consistent with previous work [Figure 2(a), inset].[32] We highlight in particular the (200) reflections of the λ (Li_2MnO_3-like) phases, observed around $Q \simeq 1.4$ Å^{-1} and indicated by an asterisk in Figure 2(a). Those reflections exhibit a "Warren-type" peak shape[69] with a relatively low intensity, suggestive of both honeycomb ordering within the *TM* layers and the presence of stacking faults (involving translation of the honeycomb-ordered layers in the *ab* plane[66]). Such planar defects are reminiscent of the stacking faults observed in O3-type Li_2MnO_3,[3,15] which have been described as a mixture of eclipsed/staggered arrangements of the Mn_6 rings along the *c* axis.[33,70] Here, stacking faults are captured by including two λ phases, each having a subtly different stacking of the Mn_6 honeycombs along the *c*-axis. An alternative model in which the two Li_2MnO_3 phases were modeled as a single O4-type phase (essentially taking the $Cmc2_1$ and $P2_1$ phases and stitching them together along c), was also considered [Figure S4]. Whilst the fits using this two-phase model and the previously-discussed three-phase model are of similar quality, the three-phase model is a more accurate representation of the true structure as the superlattice reflections expected for the O4 phase and corresponding to a doubling of the cell along the c-axis are not observed.

Additional analysis of the synchrotron PXRD data using the DIFFaX software package (implemented in TOPAS)[39,71] to refine the structure using a large cell comprising several stacking faults led to a marginally better fit ($R_{\text{w.p.}}$ = 11.8%) [Figure S5]. However, the refinement was not sufficiently improved to justify the use of such a large cell (*i.e.*, of such a large number of refinable parameters, worsening the refinement statistics).

The refined lattice parameters and site occupancies for the η and for the two λ phases in the three-phase model [Table S2] are broadly consistent with the work by Luo et al.,[32] albeit a lower Li content is obtained for the η phase. We note that the previous work did not provide Rietveld refinements, but only qualitatively compared calculated patterns to the observed data. The refined stoichiometries are $Li_{0.78}[Al_{0.02}Mn_{0.67}Ni_{0.31}]O_2$ for the η phase, which makes up approximately 82 mol % of the cathode, and Li_2MnO_3 for the λ phases, making up for 18 mol % of the cathode. While no crystalline impurity phases were detected in our samples, the total Li content in the three O2 phases was constrained to the Li content in the cathode derived from ICP and ^{7}Li NMR analysis (which is sensitive to amorphous Li-containing impurity phases, as discussed earlier), while the Mn, Ni and Al contents were constrained to their ICP values. This way, our refined compositions and phase fractions are entirely consistent with the cathode stoichiometry obtained from the combined ICP and NMR analysis. Notably, while the previous

work[32] identified a rather significant fraction of Ni in the Li layers (33%) in this material using high resolution scanning transmission electron microscopy (STEM), the inclusion of such anti-site defects in our refinements yielded a poorer fit of both the neutron and X-ray diffraction patterns ($R_{\mathrm{w.p.,PXRD}}$ = 10.6 % and $R_{\mathrm{w.p.,PND}}$ = 8.9 % for the refinement without Ni anti-sites; $R_{\mathrm{w.p.,PXRD}}$ = 13.8 % and $R_{\mathrm{w.p.,PND}}$ = 11.8 % for a representative refinement with Ni anti-sites), suggesting no such defects in our material [Figures S6 to S10]. Similarly, we found no evidence for Mn or Al anti-site defects. Refinements that included Ni in the λ-phase models were also performed, but this did not improve our fit [Figure S11]. Overall, our refinement results of LAMNO indicate good retention of the *TM* ordering present in the initial NAMNO compound in LAMNO [Supplemental Note 1], and the absence of *TM* cation migration into the Li layers during the ion exchange process.

Careful examination of the Li and *TM* slab thicknesses suggest that the η ($Li_{0.78}[Al_{0.02}Mn_{0.67}Ni_{0.31}]O_2$) and λ (Li_2MnO_3) phases cannot be located contiguously with co-planar *TM* and Li layers without considerable internal strain, as shown in Figure 2(d). The in-plane *TM*–*TM* distances, however, are very similar, suggesting that, if the phases are contained within a single particle/grain, an epitaxial arrangement of the two phases is more probable, where the (00l) layers stack on top of each other, as was suggested by Luo *et al.*[32] based on TEM analysis. This phase distribution is presumably inherited from the NAMNO precursor, where the Na and *TM* slab thicknesses are significantly different in the two P2 phases, but the *TM*–*TM* distances are similar [Table S1 and Figure S2]. However, our analysis cannot conclusively determine whether the different phases co-exist within single grains or are present in separate grains. Indeed, our Rietveld refinements suggest an approximate average crystallite size of 0.62 μm for the η phase, and of 15 nm for the λ phases, while a broad distribution of particle sizes, ranging from hundreds of nanometers to microns, is observed by scanning electron microscopy (SEM) [Figure 2(e) and S12 to S15].

DFT investigation of anti-site defect formation energies.

While our Rietveld refinements did not suggest any anti-site defects in LAMNO, for the sake of completeness, we examined whether such defects could form, at least on a local scale, by computing their formation energies [Figure 3(a) and (b)]. We calculated the formation energies of anti-sites in LAMNO, rather than NAMNO, on the basis that anti-sites were anticipated to be less stable in NAMNO due to the prismatic coordination of interlayer species in this structure. Hence, our calculations of anti-site defect formation in LAMNO represent the "worst-case scenario" of retaining such defects in the ion-exchanged material. In previous work, Luo *et al.*[32] computed the energies of three different configurations of O2-Mn_4NiO_{12}—deemed to be representative of the material after Na has been removed but before Li has been inserted into the structure[32]—in which Ni either (i) occupies the *TM* layer or (ii) occupies one of two symmetrically distinct Li layer sites. It is unclear whether this work accounted for Ni vacancies in the *TM* layer when Ni was added to the Li layer. Here, we elected to examine the energies of a large number of configurations with overall composition $Li_{2/3}Ni_{1/3}Mn_{2/3}O_2$ or Li_2MnO_3, and containing either Ni or Mn in the Li layers. These compositions are representative of the η and λ phases observed in pristine LAMNO. The calculations were conducted on cells three times the size of the O2 primitive cells and containing twelve *TM* sites arranged in a honeycomb pattern, which is the preferred ordering observed in our diffraction (as indicated by the reflections around $Q \simeq 1.4\text{Å}^{-1}$ in Figure 2(a)) and NMR results (see later). Configurations were enumerated by first moving one of the *TM* ions from a *TM* layer site to the Li layer below. Then, starting from this TM_{Li} configuration, different Li/vacancy orderings were enumerated in the Li layers. We investigated two concentrations of Ni anti-sites that are consistent with the concentrations reported by Luo *et al*, and one concentration of Mn anti-sites. Given the large number of possible

configurations of both displaced *TM* cations and Li/vacancy orderings, sampling all structures was computationally intractable and a more pragmatic approach was used instead, where at least 200 configurations were sampled randomly for each composition of interest.

The types of anti-sites considered herein are shown in Figure 3(a) for O2-$Li_{2/3}Ni_{1/3}Mn_{2/3}O_2$ and in Figure 3(b) for O2-Li_2MnO_3. For honeycomb-ordered O2-$Li_{2/3}Ni_{1/3}Mn_{2/3}O_2$, anti-sites were created by (i) swapping one or more Ni^{2+} or Mn^{4+} cation(s) in the *TM* layer with one or more Li^+ cation(s) in the Li layer —these defects are denoted as Ni_{Li}/Li_{Ni} and Mn_{Li}/Li_{Mn}, respectively—or (ii) by swapping a Li in the Li layer for a Ni and leaving a vacancy in the *TM* layer—these defects are denoted as $\square_{Ni}$. In (i) the overall Li and *TM* stoichiometry is preserved, while in (ii) one in eight Li is removed from the cell, which is charge compensated by the oxidation of one Ni. For each configuration, we calculated the difference between the formation energy of the defective structure and the convex hull at the same $Li_x[Ni_{1/3}Mn_{2/3}]O_2$ composition without a *TM* defect. This energy difference (per *TM* defect) is a measure of the energy cost of moving one *TM* cation to the Li layer in $Li_x[Ni_{1/3}Mn_{2/3}]O_2$ and is equivalent to the grand canonical defect formation energy at a constant Li chemical potential. For Li_2MnO_3, anti-sites were created by swapping Mn^{4+} in the *TM* layer for Li^+ in the Li layer without altering the overall composition. Again, this corresponded to computing the grand canonical defect formation energy at a constant Li chemical potential.

In all cases, anti-sites raise the energy of $Li_{2/3}Ni_{1/3}Mn_{2/3}O_2$, and of Li_2MnO_3 considerably. As expected, Mn anti-sites have high defect energies; in fact, such defects are rarely, if ever, observed in pristine layered oxide cathodes[72] and were not explicitly mentioned by Luo *et al.*[32] In O2-$Li_{2/3}Ni_{1/3}Mn_{2/3}O_2$, a single Ni_{Li} anti-site raises the energy of the structure by a minimum of 400 meV, while a Mn_{Li} defect raises the energy by approximately 600 meV and a Ni_{Va} defect raises the energy by approximately 300 meV [Figure 3(a), left]. In Li_2MnO_3, a single Mn_{Li} defect raises the energy by at least 300 meV [Figure 3(a), right]. On the basis of these DFT calculations, we are led to conclude that anti-site defects in the η and λ phases of LAMNO are highly unlikely.

Investigation of the local structure using solid-state NMR spectroscopy.

Having established the long-range structure of LAMNO, we next examine its local structure using ^{7}Li, ^{17}O and ^{27}Al solid-state NMR spectroscopy. The NMR spectra presented here comprise highly shifted and severely broadened resonances, a consequence of strong electron-nuclear hyperfine interactions due to the presence of paramagnetic Ni and Mn in the material and, in the case of ^{17}O and ^{27}Al, significant quadrupolar interactions.

^{7}Li NMR. The ^{7}Li Hahn-echo spectrum of pristine LAMNO [Figure 4(a)] exhibits seven broad resonances attributed to the paramagnetic LAMNO phases and centered at approximately 318 ppm (T_2-weighted integral = 15%, where T_2 is the transverse relaxation rate), 388 ppm (8%), 457 ppm (32%), 770 ppm (7%), 788 ppm (25%), 1566 ppm (1%) and 1579 ppm (5%). In addition, a sharp resonance is observed at approximately 0 ppm, corresponding to diamagnetic impurity phases (such as LiOH, Li_2CO_3, and Li_2O) at the surface of the LAMNO particles, as described earlier. The number and shifts of the paramagnetic resonances were confirmed from a pjMATPASS experiment, whereby spinning sidebands are suppressed, resulting in a “cleaner" spectrum[43] [Figure S3].

The large ^{7}Li shifts observed in the spectrum of LAMNO arise from the large paramagnetic (Fermi contact) interactions between the ^{7}Li nuclear spin and unpaired *d* electron spins from nearby open-shell *TM* species. These interactions result in the delocalization of unpaired electron spin density from the *TM d* orbital, to a bridging O *p* orbital, and eventually to an *s* orbital on the Li of interest, referred to as *TM*–O–Li bond pathways.

To assist the assignment of the LAMNO resonances, the contributions from individual neighboring open-shell *TM* ions to the overall ^{7}Li Fermi contact shift, or *TM*–O–Li bond pathway contributions, were obtained from first principles using the CRYSTAL software package[44–46] for

O2-Li_2MnO_3 and O2-$Li_{2/3}[Ni_{1/3}Mn_{2/3}]O_2$ model structures [Figure 4(b)]. We also added Al into the O2-$Li_{2/3}[Ni_{1/3}Mn_{2/3}]O_2$ structure at both Mn and Ni positions to obtain pathways involving Al (see ^{27}Al NMR). *TM*–O–Li bond pathway contributions are additive and short-range, such that the shifts of all possible Li local environments in the LAMNO phases can be predicted by summing over all the contributions from nearest- and next-nearest neighbor cations (NN and NNN, respectively). Based on the LAMNO composition derived from ICP and NMR, open-shell TM ions in the pristine cathode are predominantly Ni^{2+} or Mn^{4+} (0.91 equivalents), with a small amount of Mn^{3+} (0.09 equivalents). Unfortunately, NMR shift calculations on cells containing Mn^{3+} did not converge, and we do not include environments with Mn^{3+} neighbors in our assignments. Still, we expect our assignments to cover the vast majority of the Li environments present in the material.

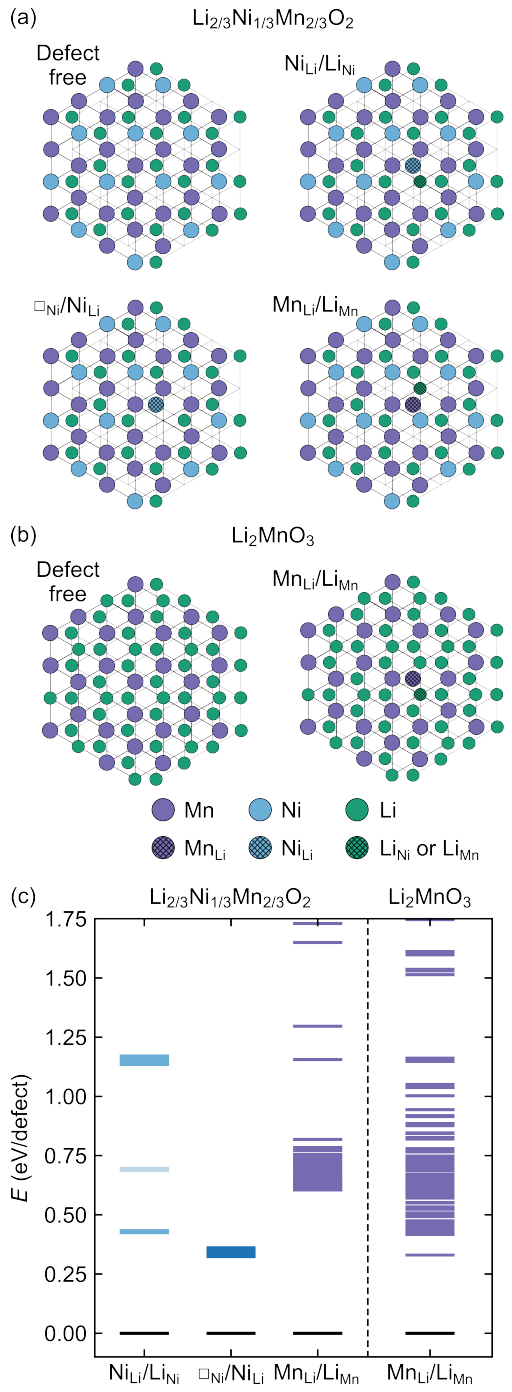

Figure 3: Schematic structures of **(a)** O2-$Li_{2/3}Ni_{1/3}Mn_{2/3}O_2$ and **(b)** O2-Li_2MnO_3 with anti-site defects. The structures are viewed down the *c* axis and show one *TM* layer and one Li layer. In **(c)**, anti-site defect energies are plotted for O2-$Li_{2/3}Ni_{1/3}Mn_{2/3}O_2$ (left) and O2-Li_2MnO_3 (right). Each line corresponds to the energy of one configuration. The zero energy corresponds to defect-free O2-$Li_{2/3}Ni_{1/3}Mn_{2/3}O_2$ (left) or defect-free O2-Li_2MnO_3 (right).

In LAMNO, Li species can occupy octahedral sites in the Li and *TM* layers. When occupying Li layer sites, Li interacts with cations in the layers above and below in two ways: on one side, Li shares a face with one cation and has six NNN cations, while on the opposite side, Li shares edges with three cations and has three NNN cations. Using the bond pathway contributions in Figure 4(b), the average Fermi contact shift of Li occupying an octahedral Li layer site between two honeycomb-ordered $Ni_{1/3}Mn_{2/3}$ layers in the η phase, and sharing a face with Mn^{4+}, is of approximately 500 ppm, as determined from two calculations using hybrid exchange-correlation functionals with 20% (Hybrid 20) and 35% (Hybrid 35) Hartree-Fock exchange (see methods), respectively. If Li instead shares a face with Ni^{2+}, its average shift is of approximately 490 ppm. If Li occupies an interlayer site in O2-Li_2MnO_3 and shares a face with Li, its average shift is of approximately 420 ppm, while if it shares a face with Mn^{4+}, its average shift is of approximately 250 ppm.

Li in a *TM* layer site has six cation NN. In this case, the NNN cations are not directly connected to Li and therefore do not contribute to its Fermi contact shift; instead, they interact with the Li nuclear magnetic moment *via* the much weaker spin dipolar hyperfine interactions, resulting in broadening of the resonance. Using a similar

method as described above, the shift of Li with six Mn NN is predicted to be of approximately 1605 ppm, while that of Li with five Mn and one Ni NN is expected at approximately 1338 ppm (see bond pathway contributions in Figure 4(b)).

Based on these predictions, the broad resonances below 1000 ppm are attributed to Li in the Li layers in the η and λ phases [Figure S16 and Tables S3 and S4]. Combining the information obtained from the bond pathway calculations and from the phase fractions derived from Rietveld refinement of the diffraction data, the resonances at 318 ppm and 770 ppm are assigned to Li in the interlayer space of the λ phases with a Mn NN and a Li NN, respectively. Those two resonances account for 15% and 7% of the total ^{7}Li signal intensity, thus the corresponding Li environments to 0.15 and 0.07 equivalents of Li in LAMNO, respectively. Three resonances are tentatively attributed to Li in the interlayer space of the η phase: 1) The 388 ppm resonance (8% of the signal or 0.08 equivalents of Li) is assigned to interlayer Li species between two honeycomb-ordered *TM* layers, where the local composition matches the 2:1 ratio of Mn:Ni required for honeycomb order. The shifts expected for Li face sharing with a Mn or Ni in the adjacent honeycomb-ordered *TM* layer only differ by 10 ppm, and as such both of these environments may contribute to the observed resonance. 2) The 457 ppm resonance (32% or 0.32 equivalents of Li) corresponds to a "dynamic average" peak, as its shift is approximately equal to the average shift (440 ppm) for all possible Li layer environments in this phase (with Mn, Ni and Al occupation probabilities equal to the bulk stoichiometries). We note that, out of all ^{7}Li resonances present in the spectrum, the linewidth and intensity of this signal at 457 ppm changes most as a function of temperature [Figure S17], which is consistent with its assignment to an average Li environment arising from fast Li-ion dynamics. 3) The 788 ppm (25%, or 0.25 equivalents of Li) resonance is assigned to Li in Mn-rich environments, for example where Mn replaces a Ni in the middle of a Mn_6 ring.

The two signals at 1566 and 1579 ppm are assigned to Li in the *TM* layers of the λ phase [Figure S18, Table S5]. The 1579 ppm signal is

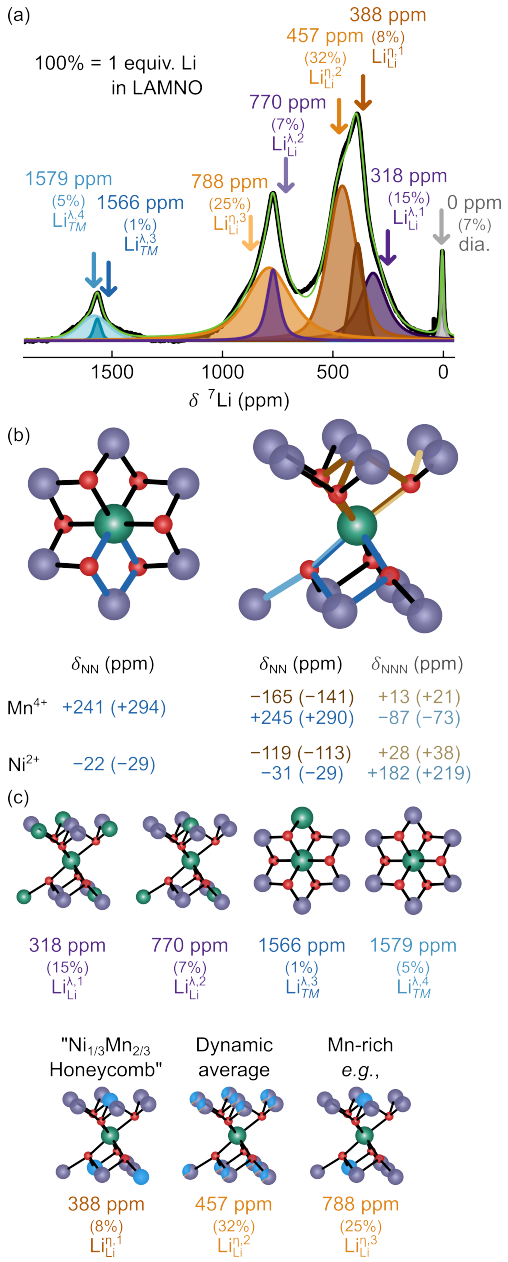

Figure 4: Solid-state ^{7}Li NMR of pristine LAMNO. In **(a)**, the bond pathway contributions to the Fermi contact shift are shown for the two distinct local Li environments: Li in the *TM* layers (left) and Li in the Li layers (right). Bond pathways are provided for nearest- and next-nearest neighbor (NN and NNN, respectively) *TM* cations; the values correspond to pathways calculated using the hybrid 20 (hybrid 35) exchange-correlation functional, with 20% (35%) Hartree-Fock exchange. The numbers in brown correspond to pathways in the layer where Li shares a face with the *TM*, while numbers in blue correspond to pathways in the layer that shares an edge with the *TM*. In **(b)**, the isotropic region of the ^{7}Li NMR Hahn-echo spectrum is shown, recorded at a field of 2.35 T under 40 kHz magic angle spinning (MAS); assignments based on the bond pathways are also highlighted. In **(c)**, the corresponding assignments to local Li environments in both the η and λ phases are shown.

ascribed to Li with six Mn^{4+} nearest-neighbors on the basis of the computed bond pathways in Figure 4(a). The 1566 ppm signal could result from Li with five Mn^{4+} and one Ni^{2+} nearest neighbors (here, denoted as $LiMn_5Ni_1$), as has been suggested in previous work on related systems,[73] but could also correspond to Li with five Mn^{4+} nearest neighbors and one Li^+ ($LiMn_5Li_1$). Indeed, our calculations suggest that the shift of Li in a $LiMn_5Ni_1$ environment is in the range of 1205 to 1470 ppm, while that of Li in a $LiMn_5Li_1$ environment is in the range of 1183 to 1441 ppm (the ranges again arising from the two levels of Hartree-Fock exchange used). Furthermore, given that our Rietveld refinement indicated that the only phase containing Li in the *TM* layers is Li_2MnO_3, and that adding a small (1%) fraction of Ni occupancy to the *TM* layer sites in the λ phases does not improve the fit [Figures S6 to S10], the 1566 ppm signal is attributed to Li in a $LiMn_5Li_1$ or "dilithium" environment, where two Li^+ ions sit directly next to each other in the *TM* layer. We also note that the signal at 1566 ppm is sharper than that at 1579 ppm (assigned to a $LiMn_6$ environment), which suggests that the corresponding Li species are involved in weaker or fewer *TM*–O–Li bond pathway interactions and is consistent with a $LiMn_5Li_1$ environment but not with a $LiMn_5Ni_1$ environment.

Having assigned each peak to a local environment, we now turn to examine the fraction of Li in each of the η and λ phases. The resonances attributed to Li in the η phase at 388 ppm, 457 ppm, and 788 ppm account for 0.08, 0.32, and 0.25 equivalents of Li, respectively. The total amount of Li in the η phase is therefore 0.08 + 0.32 + 0.25 = 0.65 equivalents, consistent with the refinement results (82 mol % $\times$ 0.78 equivalents of Li = 0.64 equivalents of Li). Furthermore, the total Li in LAMNO sitting in the Li layers of the λ phase corresponds to 0.25 equivalents, also consistent with observations. Our assignment also suggests that 0.08/0.65 = 12% of the Li in the η phase sits in environments where the Ni and Mn cations are honeycomb ordered. Hence, while honeycomb order is present, the ordered domains are quite small and only lead to low-intensity superlattice reflections in the diffraction patterns (see discussion).

Overall, our ^{7}Li NMR analysis indicates that cations in the *TM* layers of the η and λ phases are at least partially honeycomb-ordered, with evidence for domains exhibiting greater disorder, including pairs of neighboring Li^+ ions in the λ phase. In addition, the ^{7}Li NMR results are not consistent with Ni^{2+} anti-site defects in the pristine material, as these would lead to a total ^{7}Li shift of either 100 ppm or 1100 ppm for nearby Li species (depending on the bond angles and distance between the Li and the Ni anti-site), and such signals are not experimentally observed. The absence of signals from Li nearby anti-sites is in line with our diffraction and first principles results presented in the previous sections, and contrasts with the previous report on this material.[32]

^{27}Al NMR. The ^{27}Al NMR spectrum collected on pristine LAMNO consists of a broad, 'wedge-shaped' resonance whose center-of-mass lies at approximately 2300 ppm, which we attribute to Al in the *TM* layers of the η phase [Figure 5(a)]. Two additional sharp features are observed at approximately 12 ppm and 75 ppm, which account for approximately 25% and 14% of the total signal intensity, respectively [Figures 5(a),(b)]. These lower-frequency resonances are assigned to octahedral and tetrahedral Al environments in diamagnetic Al-containing impurity phase(s), most likely Al_2O_3, consistent with previous work.[74] A precise determination of which polymorph(s) of Al_2O_3 is (are) present in the sample is challenging on account of the broad line-shapes and lack of crystalline impurity phase(s) observable by diffraction. The sideband manifolds of the diamagnetic signals extend over thousands of ppm, indicating strong spin-dipolar interactions between the Al nuclei and unpaired electrons on nearby Mn species. Hence, the diamagnetic Al_2O_3 phase(s) is (are) in close proximity to (within 1-2 nanometers from) the paramagnetic, Mn-containing cathode, and likely cover(s) the surface of the particles.

Deconvolution of the wedge-shaped resonance is challenging, with multiple possible solutions, but the fit can be informed by predictions of plausible ^{27}Al Fermi contact shifts based on bond pathway analysis [Figure 5(c)]. For Al in the *TM*

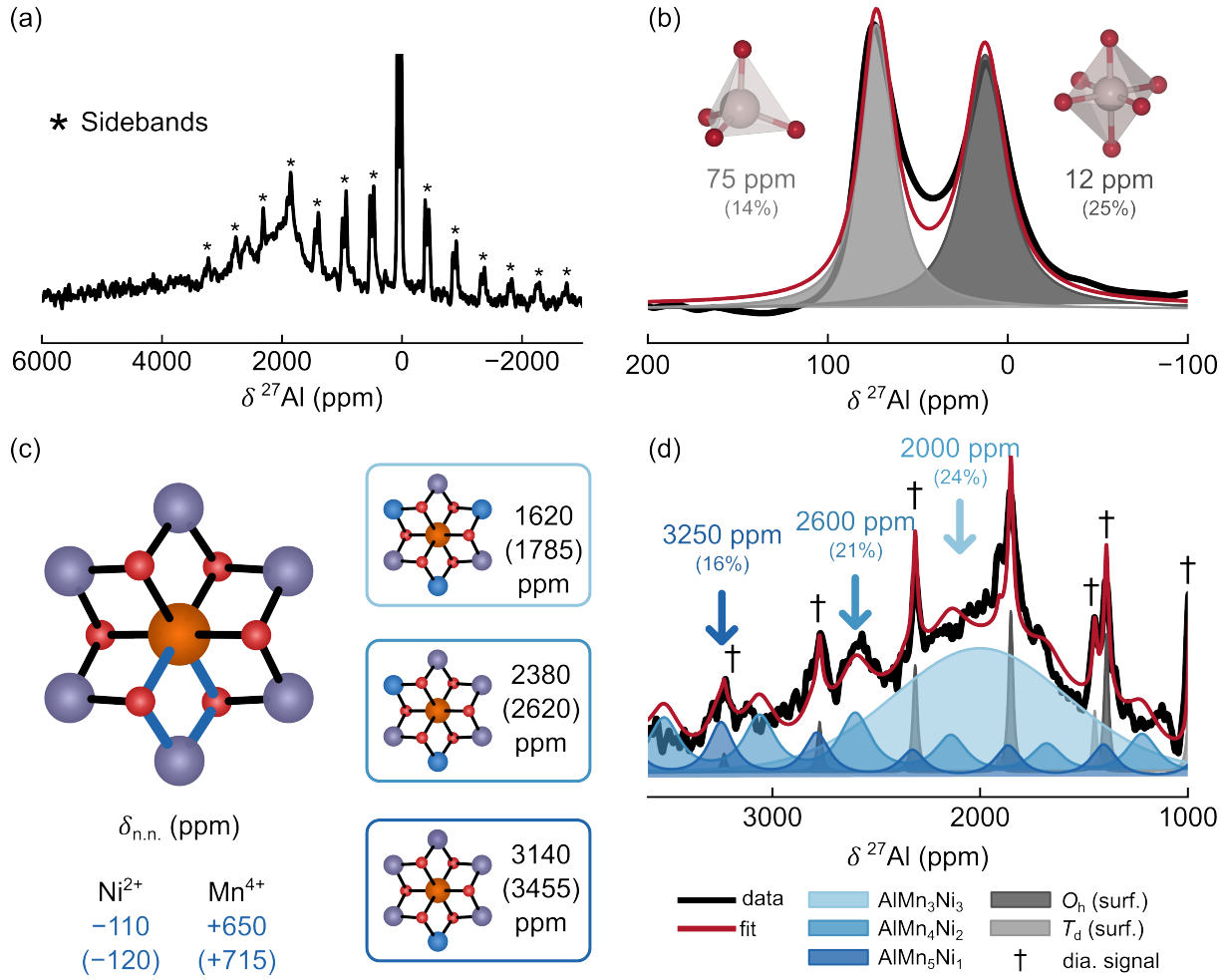

Figure 5: Solid-state ^{27}Al NMR of pristine LAMNO. In **(a)**, the overall Hahn-echo spectrum recorded at a field of 11.7 T and a MAS speed of 60 kHz is shown. In **(b)**, a fit of the isotropic diamagnetic signals is shown. Bond pathways are shown in **(c)** for nearest-neighbor (NN) *TM* cations; the values correspond to pathways calculated using the hybrid 20 (hybrid 35) exchange-correlation functional, with 20% (35%) Hartree-Fock exchange, and example configurations are shown on the right. The bond pathways were used to assist the interpretation of the paramagnetic ^{27}Al NMR signals in **(a)**, with a fit of that region of the spectrum shown in **(d)**.

layer, the predicted contribution from individual Mn^{4+} NN is between 650 and 715 ppm to the total shift (depending on the hybrid functional used in the calculation), while a Ni^{2+} NN contributes between −110 and −120 ppm [Figure 5(c)]. On the basis of these pathway contributions, the signal observed at approximately 2000 ppm is assigned to Al with three Mn and three Ni nearest neighbors, and those observed at 2600 ppm and 3250 ppm likely correspond to Al with four Mn and two Ni, and with five Mn and one Ni nearest neighbors, respectively. While the distribution of ^{27}Al resonances is close to that expected based on a random distribution of *TM* cations [Figure 5(a)], there are no environments in which Al does not have at least one Ni nearest neighbor, indicating a partial preference of Al to be coordinated by Ni.

Overall, our ^{27}Al NMR results indicate the presence of (an) amorphous surface aluminate phase(s) undetectable by diffraction methods, which account for approximately 40% of the Al content in the sample, explaining the lower-than-expected refined Al content in the Li-poor phase (0.02 equivalents instead of the targeted 0.04 equivalents) as obtained from analysis of the neutron and X-ray diffraction results presented earlier.[32] In the $Li_{2/3}[Ni_{1/3}Mn_{2/3}]O_2$ phase, Al^{3+} ions occupy *TM* sites, once again consistent with the neutron and X-ray diffraction results, with a tendency to segregate to Ni-rich regions.

^{17}O NMR. Having established the distribution

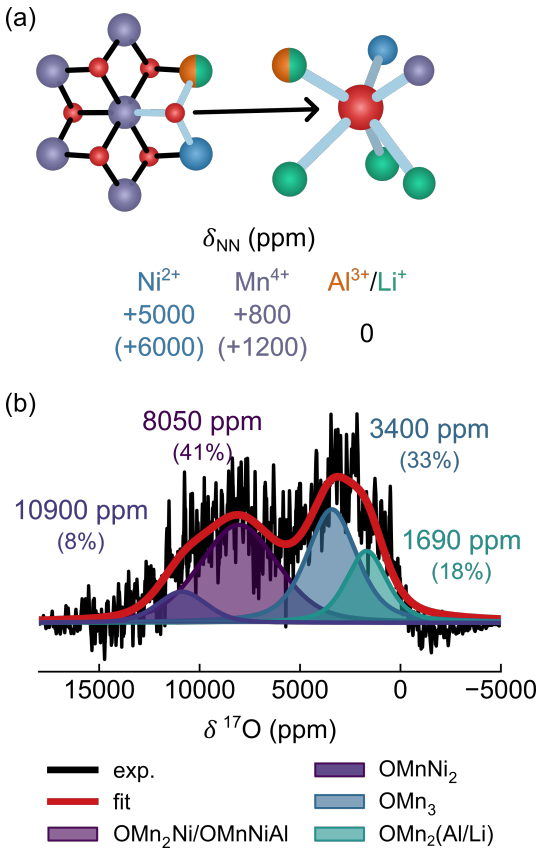

Figure 6: Solid-state ^{17}O NMR of pristine LAMNO. In **(a)**, the calculated bond pathway contributions to the ^{17}O Fermi contact shift are given for nearest-neighbors (NN) *TM* species; the values correspond to pathways calculated using the hybrid 20 (hybrid 35) exchange-correlation functional, with 20% (35%) Hartree-Fock exchange. In **(b)**, an example fit to the ^{17}O NMR spectrum of pristine LAMNO, acquired at a field of 11.7 T and MAS speed of 60 kHz, using the bond pathway derived isotropic shifts as starting points. Approximate assignments of the resonances are given underneath the spectrum.

of Li and Al local environments in LAMNO, we now turn to ^{17}O NMR. The observed chemical shift of ^{17}O species in LAMNO depends on competing paramagnetic and quadrupole-induced shift contributions, and is highly sensitive to the local geometry around the ^{17}O nucleus (bond angles and lengths), as well as the degree of ionicity or covalency of the metal-oxygen bonds.[75] Here, O^{2-} is bound to three cation species in the *TM* layers and up to three Li in the Li layers. The ^{17}O NMR spectrum obtained for pristine LAMNO comprises one severely broadened resonance whose center of mass lies at approximately 6500 ppm. The spectrum extends from approximately 0 ppm up to 12000 ppm, however, suggesting a range of local environments. We focus hereafter on the effect of the three NN cations occupying the *TM* sites, as these dominate the observed shift (Li^+ being diamagnetic). The bond pathway contribution for a Mn^{4+} NN lies between 800 and 1200 ppm (depending on the bond angle and length, as shown previously[70,75]), and that for a Ni^{2+} NN is between 5000 and 6000 ppm [Figure 6(a)].

Using these bond pathway contributions, we attribute the observed overlapping signals, in order of increasing frequency, to O^{2-} bound to, in the *TM* layer: two Mn^{4+} and one diamagnetic species (Li or Al, *e.g.*, which corresponds to the expected O^{2-} local environment in honeycomb-ordered O2-Li_2MnO_3 or λ phase), O^{2-} bound to three Mn^{4+}, O^{2-} bound to one Ni^{2+} and two Mn^{4+}, and O^{2-} bound to two Ni^{2+} and one Mn^{4+} [Figure 6(b)]. Additional simulations of all possible environments are highlighted in Figure S19. Notably, the absence of any signal in the 15000-18000 ppm range suggests no O environment with three Ni^{2+} NN, although it is also possible that the signal lifetime of these O environments is too short on the timescale of NMR data acquisition (see Discussion).

Electrochemical Results.

The initial electrochemical profile of LAMNO is similar to that of O3-type Li-rich layered oxide cathodes: the first region of the initial charge curve features a steep rise in potential, corresponding to approximately 15% of the total capacity of the cathode. This is followed by a high-potential region with a shallower slope [Figure 7], consistent with previous work on this material.[32] A large potential hysteresis is observed on subsequent discharge, with later cycles exhibiting a smoother (S-shaped) profile and a smaller (yet still considerable) hysteresis, alongside a gradual loss of capacity over the first 100 cycles.

Although the overall capacity retention remains relatively high for an anion redox cathode, there are clear signs of structure-altering processes from the electrochemical profiles. These are

perhaps most evident from the gradual decrease in the average potential of LAMNO, calculated as the average of the average potential on charge and the average potential on discharge (i.e., for a full cycle), over the first hundred cycles [Figure S20]. The average potential decay of our material, that of Luo et al.,[32] and for a series of Li- and Mn-rich O3-type cathodes, are compared in Table S6. Unfortunately, none of the previous studies have indicated whether the potential decay was computed for a full cycle or per half cycle (only charge or only discharge), and we hereafter assume the former. Our full cycle potential decay is slightly higher than that reported by Luo et al., particularly after the first 10 cycles; we note, however, that a higher rate and narrower potential window was used in that previous work, which reduces cathode utilization and likely mitigates degradation. Beyond the first 10 cycles, the potential decay stabilizes and becomes as low as -0.5 mV per full cycle. From cycle 10 to 100, the average potential of LAMNO on charge gradually increases from one cycle to the next, whilst the average discharge potential gradually decreases. We suggest that the gradual increase in charge potential arises from an increase in the impedance of LAMNO, rather than structure-altering processes, which would likely manifest as a sudden change to the average potential (for example, as seen between the first and second cycle average potentials of LAMNO, Figure S20). We note also that, despite previous claims, the potential decay in LAMNO is comparable to other O3 cathodes for the first cycle, but then becomes much smaller on subsequent cycles, further hinting at irreversible structural changes taking place in LAMNO over the first cycle [Figure S20 and Table S6].

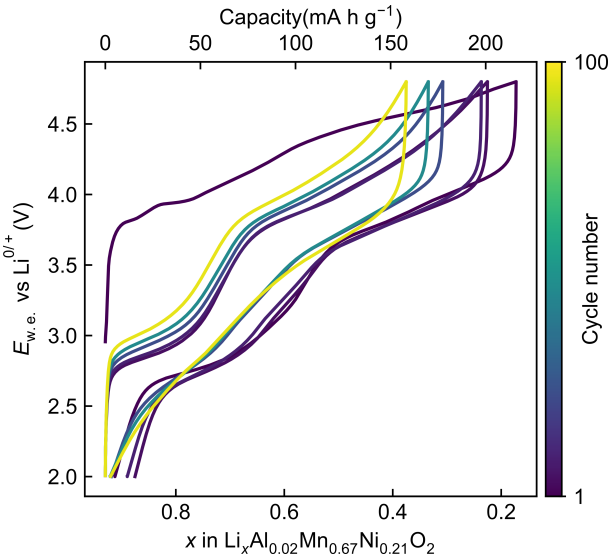

Figure 7: electrochemical profiles over the first 100 cycles of LAMNO cycled in a half-cell configuration at 298 K and a rate of 20 mA g^{-1} between 2.0 and 4.8 V using $LiPF_6$ in a 1:1:1 v/v solution of EC/DMC/DEC as the electrolyte.

Discussion

Our results on as-prepared LAMNO reveal a similar long-range structure as that reported by Luo *et al.*:[32] the LAMNO cathode comprises chemically distinct O2-type phases, the η phase ($Li_{0.78}[Al_{0.02}Mn_{0.67}Ni_{0.31}]O_2$) and λ phase(s) (Li_2MnO_3) containing stacking faults (that can be modeled with two simple stacking sequences), as determined from neutron and synchrotron X-ray diffraction. The electrochemical behavior of our LAMNO material is also consistent with that reported by Luo *et al.*, which suggests very similar local structures in our materials. Despite those apparent similarities, we diverge on the origin of the remarkable electrochemical performance of LAMNO, as explained below.

Firstly, Luo *et al.* synthesized NAMNO (the precursor to LAMNO) using 13 mol.% excess of transition metal carbonates, which they justified as necessary to form *TM* anti-site defects in the layered oxide product. In the present work, we instead used stoichiometric amounts of the precursors and, to the best of our knowledge, obtained a very similar product, as noted earlier. We rationalize these results by possible hydration of the carbonates prepared by Luo *et al.*, requiring additional precursor mass for a similar *TM* content. Indeed, $MnCO_3$ and $NiCO_3$ are strongly hygroscopic[76] and we have found that such compounds require temperatures of at least 120 °C to remove the water of crystallization. Luo *et al.* instead used 90 °C to dry their precursors and those may have remained partially hydrated.

Secondly, Luo *et al.* observed ordered spots in the Li layers of LAMNO using TEM, which they ascribed to anti-site defects, TM_{Li}. TM

cations in the Li layer is inconsistent with our Rietveld refinements [Figure S11]. Furthermore, our DFT calculations indicate that as-prepared LAMNO is unlikely to contain anti-site defects in either the η or λ phases. DFT calculations by Luo *et al.* of excess Ni in delithiated MnO_3 also predict a preference for the TM layer as opposed to the Li layer. TM anti-sites in the prismatically coordinated sites of the Na layers of the P2 NAMNO precursor is also highly unlikely, due to the unfavorable coordination and the size mismatch between Na^+ and the *TM* cations. While the NAMNO precursor could contain local O2-stackings, in which a *TM* cation could occupy an octahedral interlayer site, our DFT results indicate that the formation of such octahedral anti-site defects is unfavorable when Li is present in the interlayer space [Figure 3(c)], likely on account of sharing a face with a neighboring *TM* cation.

Our structural characterization results indicate partial honeycomb ordering on the *TM* layers in the η and λ phases. In the η phase, such ordering is not immediately apparent from the diffraction results, but is evident from the NMR results. The ^{7}Li NMR spectrum indicates that a fraction of the Li (0.08 equivalents out of 0.65, or approximately 12% of the Li) in the η phase occupies Li-layer sites with a honeycomb arrangement of neighboring *TM* cations in the adjacent layers. The absence of long-range honeycomb order likely stems primarily from the presence of approximately 2% Al in the *TM* sublattice [Figure 8]. Starting from a perfect honeycomb ordering (*i.e.*, a 2:1 ratio of Mn:Ni), either a Ni or Mn is replaced with an Al cation. On the basis of the *TM* layer composition, $Ni_{0.31}Al_{0.02}Mn_{0.67}$, we suggest that Ni is replaced by Al. However, the inclusion of Al in the *TM* layers does not result from a simple substitution of Ni: for example, if Al were to replace a Ni in the center of a Mn_6 ring, one would observe a signal at 3900-4290 ppm (based on our bond pathway calculations; Figure 5(c)), which is not the case. Instead, we find that Al occupies *TM* sites with at least one Ni nearest neighbor. Hence, other substitution schemes must be considered. For instance, if instead of replacing Ni, Al were to replace Mn, and Mn then replaces a Ni according to the average composition of the *TM* layer, a "defective honeycomb" structure would develop. Clearly, Mn could substitute either the nearest Ni, yielding a Al[Ni_2Mn_4] environment, or a next-nearest Ni, yielding a Al[Ni_3Mn_3] environment [Figure 8(a), (b), (c) and (d)]. Furthermore, in a honeycomb, one might expect the presence of anti-phase boundaries: extended defects that separate two translational variants of well-ordered domains [Figure 8(e)]. These anti-phase boundaries are likely formed during synthesis as two honeycomb-ordered domains impinge on each other as they grow. Under this scheme, it is possible for Al to acquire only one Ni nearest neighbor [Figure 8(e) and (f)]. These ordering scenarios are depicted in Figure 8, and additional examples of defective honeycomb structures are depicted in Figures S21 to S23.

Overall, the introduction of Al can lead to a departure from a pure honeycomb arrangement of the cations in the *TM* layers in the η phase. Partial and short-range honeycomb ordering in this phase is consistent with the ^{7}Li, ^{27}Al and ^{17}O NMR results [Figures 4, 5 and 6], and with the low intensity, broad reflection at $Q \simeq 1.4$Å^{-1} in the synchrotron XRD pattern [Figure 2(a)]. In addition to the loss of long-range in-plane order due to Al incorporation, stacking faults of the *TM* layers are also likely to be present in the ion-exchanged structure; these, too, will reduce the extent of long-range order [Figures S24 to S26][67] and may further explain the weak superstructure reflections observed in the synchrotron XRD pattern.

Partial honeycomb-ordering is also evident in the λ phases of LAMNO. Once again, this is supported by the reflections around $Q \simeq 1.4$Å^{-1} in the synchrotron XRD data. Furthermore, the signal observed at 1579 ppm in the ^{7}Li NMR spectrum provides direct evidence for the presence of Li in the *TM* layers surrounded by six Mn nearest neighbors. This honeycomb ordering, as in the η phase, is far from perfect. This is evident from the presence of dilithium (Li[Mn_5Li]) environments revealed by the 1566 ppm signal in the ^{7}Li NMR spectrum. Those dilithium environments may arise from anti-phase boundaries in the NAMNO precursor, as indicated by ^{7}Li NMR [Figure S27], formed

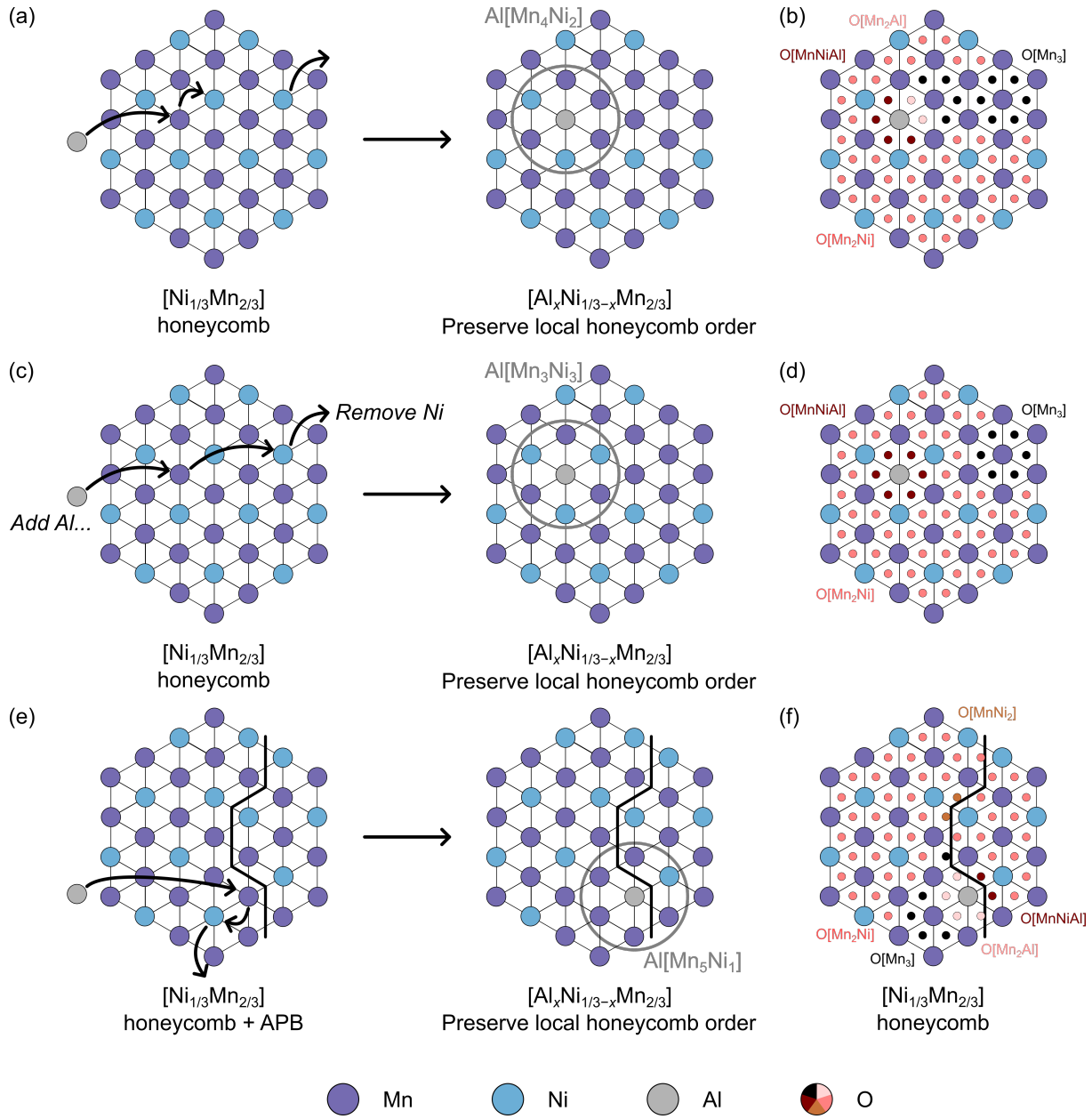

Figure 8: The effect of Al doping on local Al and O environments in the η phase of LAMNO. In **(a)**, the perfect $Ni_{1/3}Mn_{2/3}$ ordering is shown, viewed directly down the c-axis, onto the *TM* plane. When an Al replaces a Mn site and the displaced Mn replaces a nearby Ni, an ordering as shown on the right develops, creating an $Al[Ni_2Mn_4]$ environment. The corresponding O environments in the layer are highlighted in **(b)**. A similar scheme is shown in **(c)**, with the displaced Mn now replacing a different Ni center, yielding an $Al[Ni_3Mn_3]$ environment; the corresponding O environments are given in **(d)**. In **(e)**, the region around an anti-phase boundary (APB) is shown, with perfect honeycomb ordering on each side of this boundary. On replacing a Mn with Al and then replacing Ni with Mn, a $Al[Ni_1Mn_5]$ environment forms. The corresponding O environments are shown in **(f)**.

during the initial high-temperature solid-state reaction. We illustrate the formation of dilithium and dimanganese environments at anti-phase boundaries in Figure 9(a). It is also possible that, instead of extended anti-phase boundaries, the dilithium environments occur as isolated point defects (*i.e.*, Li/Mn anti-sites). Discerning between anti-phase boundaries and localized defects is experimentally challenging and are beyond the scope of this work. Based on the quantification of the ^{7}Li NMR results, dilithium environments in the λ phase(s) make up for 1% of the total Li content (*i.e.*, 0.01 equivalents of Li), while Li in perfect honeycomb environments

($LiMn_6$) in these *TM* layers make up for 5% of the total Li content in LAMNO. From this, we deduce that approximately 16% of the Li in the *TM* layers of the λ phase have a Li nearest neighbor, with important consequences on the electrochemical behavior.

Finally, we relate the phase composition and structure of LAMNO to its electrochemical performance. Our LAMNO cathode comprises 82% of an η phase with chemical formula $Li_{0.78}[Al^{3+}_{0.02}Mn^{3+}_{0.12}Mn^{4+}_{0.55}Ni^{2+}_{0.31}]O_2$ based on charge balancing and the relative redox potentials of the $Ni^{2+/3+}$ and $Mn^{3+/4+}$ couples. This distribution of oxidation states means that 0.74 equivalents of Li can be removed from this phase: 0.12 from the oxidation of $Mn^{3+} \rightarrow Mn^{4+}$, and 0.62 from the oxidation of $Ni^{2+} \rightarrow Ni^{4+}$. This corresponds to a total theoretical capacity of 214 mAh g^{-1}, which when scaled by the phase fraction becomes 160 mAh g^{-1} or 0.56 equivalents of Li. The theoretical capacity of the λ phase is approximately 459 mAh g^{-1} (assuming full removal of Li in Li_2MnO_3 from anion redox), and when scaled by the phase fraction amounts to 115 mAh g^{-1} or 0.33 equivalents of Li.

Based on the observed first charge capacity of 216 mA h g^{-1} upon cycling over a wide potential window of 2.0–4.8 V, it is clear that not all of the Li can be extracted from LAMNO. Given that the η phase is structurally similar to the O2-$Li_{2/3}Ni_{1/3}Mn_{2/3}O_2$ compound first reported by Paulsen *et al.*,[77] we suggest that almost all of the available theoretical capacity in this material (corresponding to the extraction of 0.67 equivalents of Li, or 130 mA h g^{-1}) can be and is extracted at least on the initial charge. We note also that the shape of the LAMNO electrochemical profile is similar to the full electrochemical profile of O2-$Li_{2/3}Ni_{1/3}Mn_{2/3}O_2$ between 2.0 and 4.2 V, also suggesting that a large fraction of the capacity of LAMNO comes from the η phase. As such, the capacity limitations observed from LAMNO stem primarily from the λ phase.

One possibility for the difficulty in removing Li from the λ phase arises from the evolution of the dilithium environments during cycling. On extracting Li species from dilithium environments, divacancies are expected to form in the *TM* layers [Figure 9(a) and (b)]. As with Li hopping in the interlayer space,[78,79] these divacancies enable low-energy pathways for in-plane *TM* migration as the Coulombic repulsion experienced by the *TM* is significantly lower when migrating into the tetrahedral transition state site that does not share faces with any *TM* atom [Figure 9(c)]. In turn, a lower barrier for *TM* migration is expected to increase the mobility of Mn within the *TM* layers of Li_2MnO_3, enabling densification. We suggest that densification of the λ-phase accounts for the significant potential decay observed for LAMNO during the first cycle, which is comparable to many O3 cathodes [Table S7]. A follow-up study is underway that explores the charge compensation mechanisms and structural rearrangements taking place during the first few cycles, providing additional insight into the remarkable cycling stability of LAMNO compared to other anion redox cathodes.

Conclusion

$Li_{1.20}Al_{0.02}Mn_{0.67}Ni_{0.21}O_2$ (LAMNO) is an O2-type layered oxide cathode, previously reported with excellent electrochemical performance for an anion redox material, with little potential fade and minimal irreversible capacity losses.[32] In previous work, the cathode was found to comprise a Li-stoichiometric and Li_2MnO_3-like phase mixture, but details of its local structure remained poorly understood. Meanwhile, its exceptional electrochemical performance was ascribed to the presence of *TM* anti-site defects in the Li layers pinning the honeycomb-ordered layers and ensuring good structural stability during electrochemical cycling. In the present work, we conducted a detailed structural characterization of the as-prepared LAMNO material using synchrotron X-ray diffraction, neutron diffaction, and multinuclear (^{7}Li, ^{17}O and ^{27}Al) solid-state NMR spectroscopy. Our results confirm the presence of two distinct phases but with a lower overall Li content than previously reported. The two components were found to be Li_2MnO_3 (which we term the λ-phase, comprising 18 mol.%

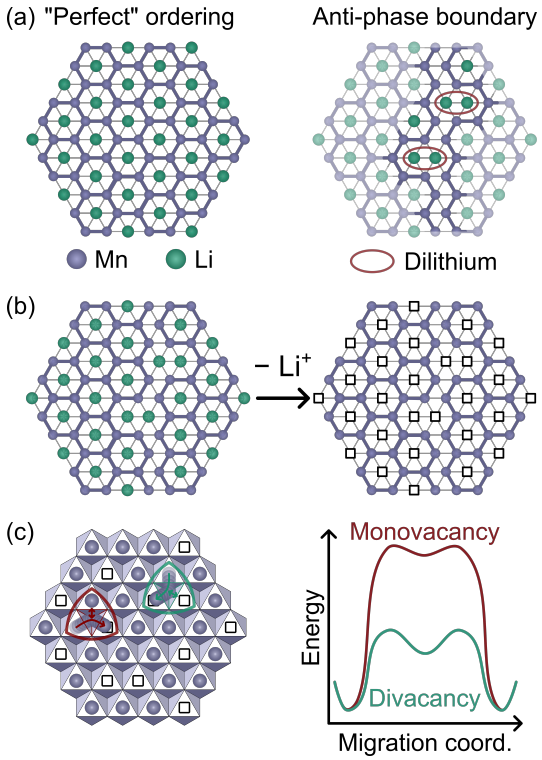

Figure 9: Impact of in-plane *TM*/vacancy ordering on *TM* migration. In **(a)**, a *TM* layer with perfect honeycomb-ordered (left) and a honeycomb-ordered with anti-phase boundary (right) are shown, with the dilithium environments highlighted. In **(b)**, the effect of removing Li species from anti-phase boundary regions is shown, while **(c)** highlights the expected impact of divacancies in the *TM* layer on the energy barrier for in-plane *TM* migration, compared to the monovacancy mechanism.

of LAMNO) and $Li_{0.78}[Al_{0.02}Mn_{0.67}Ni_{0.31}]O_2$ (the η-phase, 82 mol.%), both of which have the O2 stacking. We find no evidence for the previously-reported Ni anti-site defects and instead identify the presence of partial honeycomb ordering in the *TM* layers of the η and λ phases. In particular, our NMR results highlight a clear deviation from a random distribution of transition metals, but the absence of clear reflections in X-ray and neutron diffraction suggest that this ordering is not long-range. Further, our ^{7}Li NMR results reveal the presence of "dilithium" environments in the *TM* layers of the λ (Li_2MnO_3) phases, where Li has five Mn^{4+} and one Li^+ nearest neighbor. We propose several structural models consistent with our results, indicating that Al cations disrupt perfect honeycomb ordering in the η phase, whilst anti-phase boundaries and stacking faults disrupt this ordering in the λ phase. Finally, we suggest that the presence of dilithium environments likely has a significant effect on the electrochemical performance of LAMNO.

Supporting Information

The Supporting Information is available free of charge at ...

The SI contains: a detailed experimental, additional PND and XRD Rietveld refinements, SEM results, additional electrochemical results, additional ^{7}Li NMR results, details about the NMR shift calculations, and *TM* ordering schemes. All raw data and scripts for processing are located on Materials Commons, with DOI 10.13011/m3-ydfw-6495.

Acknowledgements

E.N.B., R.J.C. and A.V.d.V. acknowledge funding from the Office of Naval Research under grant N00014-23-1-2333. E.N.B. acknowledges the ILL for beamtime under proposal number 5-23-812 (https://doi.ill.fr/10.5291/ILL-DATA.5-23-812). E.N.B. also wishes to acknowledge Prof. Claire Villevieille for assistance with access to neutron data and acquiring time at the beam. This research made use of the shared facilities of the NSF Materials Research Science and Engineering Center at UC Santa Barbara (NSF-DMR 2308708). The UC Santa Barbara MRSEC is a member of the Materials Research Facilities Network (www.mrfn.org).

CRediT Statement

E.N.B., R.J.C. and A.V.d.V. designed the research and performed experimental and theoretical data analysis. E.N.B. conducted the materials synthesis, electrochemical tests, X-ray and neutron diffraction, NMR experiments, magnetometry and DFT calculations, and their related data analyses. E.A.L. and E.N.B conducted the SEM and ICP measurements and analysis.

E.N.B., with significant help from O.K. and E.S., collected the neutron diffraction data. R.J.C. and A.V.d.V. supervised the work. All authors discussed the results; E.N.B., R.J.C. and A.V.d.V. wrote and edited the manuscript; E.A.L., O.K. and E.S. assisted with editing and commenting of the manuscript.

References

(1) Rozier, P.; Sathiya, M.; Paulraj, A.-R.; Foix, D.; Desaunay, T.; Taberna, P.-L.; Simon, P.; Tarascon, J.-M. Anionic redox chemistry in Na-rich Na2Ru1-ySnyO3 positive electrode material for Na-ion batteries. *Electrochemistry Communications* **2015**, *53*, 29–32, Publisher: Elsevier.

(2) Lu, Z.; MacNeil, D. D.; Dahn, J. R. Layered Cathode Materials Li[NixLi(1/3-2x/3)Mn(2/3-x/3)]O2 for Lithium-Ion Batteries. *Electrochemical and Solid-State Letters* **2001**, *4*, A191, Publisher: IOP Publishing.

(3) Thackeray, M. M.; Kang, S.-H.; Johnson, C. S.; Vaughey, J. T.; Benedek, R.; Hackney, S. A. Li2MnO3-stabilized LiMO2 (M = Mn, Ni, Co) electrodes for lithium-ion batteries. *Journal of Materials Chemistry* **2007**, *17*, 3112–3125, Publisher: The Royal Society of Chemistry.

(4) Ma, C.; Alvarado, J.; Xu, J.; Clément, R. J.; Kodur, M.; Tong, W.; Grey, C. P.; Meng, Y. S. Exploring Oxygen Activity in the High Energy P2-Type Na0.78Ni0.23Mn0.69O2 Cathode Material for Na-Ion Batteries. *Journal of the American Chemical Society* **2017**, *139*, 4835–4845, Publisher: American Chemical Society.

(5) House, R. A.; Maitra, U.; Pérez-osorio, M. A.; Lozano, J. G.; Jin, L.; Somerville, J. W.; Duda, L. C.; Nag, A.; Walters, A.; Zhou, K.; Roberts, M. R.; Bruce, P. G. Superstructure control of first-cycle voltage hysteresis inO-redox cathodes. *Nature* **2019**, *577*, 502–508.

(6) Kim, E. J.; Maughan, P. A.; Bassey, E. N.; Clément, R. J.; Ma, L. A.; Duda, L. C.; Sehrawat, D.; Younesi, R.; Sharma, N.; Grey, C. P.; Armstrong, A. R. Importance of Superstructure in Stabilizing Oxygen Redox in P3-Na0.67Li0.2Mn0.8O2. *Advanced Energy Materials* **2022**, *12*, 2102325, Publisher: John Wiley & Sons, Ltd.

(7) Zhang, M.; Kitchaev, D. A.; Lebens-Higgins, Z.; Vinckeviciute, J.; Zuba, M.; Reeves, P. J.; Grey, C. P.; Whittingham, M. S.; Piper, L. F. J.; Van der Ven, A.; Meng, Y. S. Pushing the limit of 3d transition metal-based layered oxides that use both cation and anion redox for energy storage. *Nature Reviews Materials 2022* **2022**, *7*, 522–540, Publisher: Nature Publishing Group ISBN: 0123456789.

(8) Bassey, E. N.; Nguyen, H.; Insinna, T.; Lee, J.; Barra, A.-L.; Cibin, G.; Bencok, P.; Clément, R. J.; Grey, C. P. Strong Magnetic Exchange Interactions and Delocalized Mn–O States Enable High-Voltage Capacity in the Na-Ion Cathode P2–Na0.67[Mg0.28Mn0.72]O2. *Chemistry of Materials* **2024**, Publisher: American Chemical Society.

(9) Sathiya, M.; Rousse, G.; Ramesha, K.; Laisa, C. P.; Vezin, H.; Sougrati, M. T.; Doublet, M.-L.; Foix, D.; Gonbeau, D.; Walker, W.; Prakash, A. S.; Ben Hassine, M.; Dupont, L.; Tarascon, J.-M. Reversible anionic redox chemistry in high-capacity layered-oxide electrodes. *Nature Materials* **2013**, *12*, 827–835.

(10) Koga, H.; Croguennec, L.; Ménétrier, M.; Douhil, K.; Belin, S.; Bourgeois, L.; Suard, E.; Weill, F.; Delmas, C. Reversible Oxygen Participation to the Redox Processes Revealed for $Li_{1.20}Mn_{0.54}Co_{0.13}Ni_{0.13}O_2$. *Journal of The Electrochemical Society* **2013**, *160*, A786–A792, Publisher: The Electrochemical Society.

(11) Seo, D.-H.; Lee, J.; Urban, A.; Malik, R.; Kang, S.; Ceder, G. The structural and chemical origin of the oxygen redox activity

in layered and cation-disordered Li-excess cathode materials. *Nature Chemistry* **2016**, *8*, 692–697, Publisher: Nature Publishing Group.

(12) Luo, K.; Roberts, M. R.; Hao, R.; Guerrini, N.; Pickup, D. M.; Liu, Y.-S.; Edström, K.; Guo, J.; Chadwick, A. V.; Duda, L. C.; Bruce, P. G. Charge-compensation in 3d-transition-metal-oxide intercalation cathodes through the generation of localized electron holes on oxygen. *Nature Chemistry* **2016**, *8*, 684–691.

(13) Assat, G.; Tarascon, J.-M. Fundamental understanding and practical challenges of anionic redox activity in Li-ion batteries. *Nature Energy* **2018**, *3*, 373–386, Publisher: Nature Publishing Group.

(14) Radin, M. D.; Vinckeviciute, J.; Seshadri, R.; Van der Ven, A. Manganese oxidation as the origin of the anomalous capacity of Mn-containing Li-excess cathode materials. *Nature Energy* **2019**, *4*, 639–646, Publisher: Nature Publishing Group.

(15) House, R. A.; Rees, G. J.; Pérez-Osorio, M. A.; Marie, J.-J.; Boivin, E.; Robertson, A. W.; Nag, A.; Garcia-Fernandez, M.; Zhou, K.-J.; Bruce, P. G. First-cycle voltage hysteresis in Li-rich 3d cathodes associated with molecular O2 trapped in the bulk. *Nature Energy* **2020**, *5*, 777–785, Publisher: Nature Publishing Group.

(16) Vinckeviciute, J.; Kitchaev, D. A.; Ven, A. V. d. A Two-Step Oxidation Mechanism Controlled by Mn Migration Explains the First-Cycle Activation Behavior of Li2MnO3-Based Li-Excess Materials. *Chemistry of Materials* **2021**, *33*, 1625–1636, Publisher: American Chemical Society.

(17) Kitchaev, D. A.; Vinckeviciute, J.; Van Der Ven, A. Delocalized Metal-Oxygen π-Redox Is the Origin of Anomalous Nonhysteretic Capacity in Li-Ion and Na-Ion Cathode Materials. *J. Am. Chem. Soc* **2021**, *143*, 1908–1916, Publisher: UTC.

(18) Hu, K.; Tang, H.; Zheng, B.; Yu, L.; Xiong, F.; Li, H.; Qiu, L.; Wan, F.; Song, Y.; Zhong, B.; Wu, Z.; Guo, X. Constructing Targeted Strong Nb4d-O2p-Li2s Configurations to Obtain Excellent Energy Density and Long Life for Li-Rich Cathodes. *Angewandte Chemie International Edition* **2025**, *64*, e202413563, _eprint: https://onlinelibrary.wiley.com/doi/pdf/10.1002/anie.202

(19) Zuo, W.; Qiu, J.; Liu, X.; Ren, F.; Liu, H.; He, H.; Luo, C.; Li, J.; Ortiz, G. F.; Duan, H.; Liu, J.; Wang, M.-S.; Li, Y.; Fu, R.; Yang, Y. The stability of P2-layered sodium transition metal oxides in ambient atmospheres. *Nature Communications* **2020**, *11*, 3544, Publisher: Nature Publishing Group.

(20) Clément, R. J.; Lun, Z.; Ceder, G. Cation-disordered rocksalt transition metal oxides and oxyfluorides for high energy lithium-ion cathodes. *Energy and Environmental Science* **2020**, *13*, 345–373, Publisher: Royal Society of Chemistry.

(21) Kang, S.; Lee, S.; Lee, H.; Kang, Y.-M. Manipulating disorder within cathodes of alkali-ion batteries. *Nature Reviews Chemistry* **2024**, 1–18, Publisher: Nature Publishing Group.

(22) Van Der Ven, A.; See, K. A.; Pilon, |. L. Hysteresis in electrochemical systems. *Battery Energy* **2022**, 20210017, Publisher: John Wiley & Sons, Ltd.

(23) Bassey, E. N.; Reeves, P. J.; Jones, M. A.; Lee, J.; Seymour, I. D.; Cibin, G.; Grey, C. P. Structural Origins of Voltage Hysteresis in the Na-Ion Cathode P2–Na0.67[Mg0.28Mn0.72]O2: A Combined Spectroscopic and Density Functional Theory Study. *Chemistry of Materials* **2021**, *33*, 4890–4906.

(24) Boivin, E.; House, R. A.; Pérez-Osorio, M. A.; Marie, J. J.; Maitra, U.; Rees, G. J.; Bruce, P. G. Bulk O2 formation and Mg displacement explainO-redox in Na0.67Mn0.72Mg0.28O2. *Joule* **2021**, *5*, 1267–1280, Publisher: Cell Press.

(25) House, R. A.; Marie, J.-J.; Pérez-Osorio, M. A.; Rees, G. J.; Boivin, E.; Bruce, P. G. The role of O2 inO-redox cathodes for Li-ion batteries. *Nature Energy* **2021**, *6*, 781–789, Publisher: Nature Publishing Group.

(26) Zhang, Y.; Wu, M.; Ma, J.; Wei, G.; Ling, Y.; Zhang, R.; Huang, Y. Revisiting the Na2/3Ni1/3Mn2/3O2 Cathode: Oxygen Redox Chemistry and Oxygen Release Suppression. *ACS Central Science* **2020**, *6*, 232–240, Publisher: American Chemical Society.

(27) Ren, J.; Zhu, H.; Fang, Y.; Li, W.; Lan, S.; Wei, S.; Yin, Z.; Tang, Y.; Ren, Y.; Liu, Q. Typical cathode materials for lithium-ion and sodium-ion batteries: From structural design to performance optimization. *Carbon Neutralization* **2023**, *2*, 339–377, _eprint: https://onlinelibrary.wiley.com/doi/pdf/10.1002/cnl2.62.

(28) Eum, D. et al. Voltage decay and redox asymmetry mitigation by reversible cation migration in lithium-rich layered oxide electrodes. *Nature Materials* **2020**, *19*, 419–427, Publisher: Nature Research.

(29) Cao, X.; Li, H.; Qiao, Y.; Jia, M.; He, P.; Cabana, J.; Zhou, H. Achieving stable anionic redox chemistry in Li-excess O2-type layered oxide cathode via chemical ion-exchange strategy. *Energy Storage Materials* **2021**, *38*, 1–8.

(30) Cao, X.; Qiao, Y.; Jia, M.; He, P.; Zhou, H. Ion-Exchange: A Promising Strategy to Design Li-Rich and Li-Excess Layered Cathode Materials for Li-Ion Batteries. *Advanced Energy Materials* **2022**, *12*, 2003972.

(31) McColl, K.; Coles, S. W.; Zarabadi-Poor, P.; Morgan, B. J.; Islam, M. S. Phase segregation and nanoconfined fluid O2 in a lithium-rich oxide cathode. *Nature Materials* **2024**, *23*, 826–833, Publisher: Nature Publishing Group.

(32) Luo, D. et al. A Li-rich layered oxide cathode with negligible voltage decay. *Nature Energy* **2023**, *8*, 1078–1087, Publisher: Nature Publishing Group.

(33) Bréger, J.; Jiang, M.; Dupré, N.; Meng, Y. S.; Shao-Horn, Y.; Ceder, G.; Grey, C. P. High-resolution X-ray diffraction, DIFFaX, NMR and first principles study of disorder in the Li 2MnO 3-Li[Ni 1/2Mn 1/2]O 2 solid solution. *Journal of Solid State Chemistry* **2005**, *178*, 2575–2585, Publisher: Academic Press.

(34) Yoon, W.-S.; Iannopollo, S.; Grey, C. P.; Carlier, D.; Gorman, J.; Reed, J.; Ceder, G. Local Structure and Cation Ordering in O3 Lithium Nickel Manganese Oxides with Stoichiometry LiNixMn2-x/3Li1-2x/3O2 NMR Studies and First Principles Calculations. **2003**,

(35) Thompson, S. P.; Parker, J. E.; Potter, J.; Hill, T. P.; Birt, A.; Cobb, T. M.; Yuan, F.; Tang, C. C. Beamline I11 at Diamond: A new instrument for high resolution powder diffraction. *Review of Scientific Instruments* **2009**, *80*, 075107, Publisher: American Institute of PhysicsAIP.

(36) Tartoni, N.; Thompson, S.; Tang, C.; Willis, B.; Derbyshire, G.; Wright, A.; Jaye, S.; Homer, J.; Pizzey, J.; Bell, A.; IUCr High-performance X-ray detectors for the new powder diffraction beamline I11 at Diamond. *Journal of Synchrotron Radiation* **2008**, *15*, 43–49, Publisher: International Union of Crystallography.

(37) Rietveld, H. M. Line profiles of neutron powder-diffraction peaks for structure refinement. *Acta Crystallographica* **1967**, *22*, 151–152.

(38) Rietveld, H. M. A profile refinement method for nuclear and magnetic structures. *Journal of Applied Crystallography* **1969**, *2*, 65–71, Publisher: International Union of Crystallography.

(39) Coelho, A. A. *TOPAS* and *TOPAS-Academic* : an optimization program integrating computer algebra and crystallographic

objects written in C++. *Journal of Applied Crystallography* **2018**, *51*, 210–218, Publisher: International Union of Crystallography.

(40) Coelho, A. TOPAS-Academic: General Profile and Structure Analysis Software for Powder Diffraction Data. **2007**, Place: Brisbane, Australia.

(41) Suard, E.; Hewat, A. The Super-D2B project at the ILL: Neutron News: Vol 12, No 4. *Neutron News* **2001**, *12*, 30–33.

(42) Wasylishen,R.; Ashbrook, S.; Wimperis, S. *NMR of Quadrupolar Nuclei in Solid Materials*; Wiley, 2012; pp 17–44.

(43) Hung, I.; Zhou, L.; Pourpoint, F.; Grey, C. P.; Gan, Z. Isotropic high field NMR spectra of Li-ion battery materials with anisotropy >1 MHz. *Journal of the American Chemical Society* **2012**, *134*, 1898–1901, ISBN: 0002-7863.

(44) Clément, R. J.; Pell, A. J.; Middlemiss, D. S.; Strobridge, F. C.; Miller, J. K.; Whittingham, M. S.; Emsley, L.; Grey, C. P.; Pintacuda, G. Spin-Transfer Pathways in Paramagnetic Lithium Transition-Metal Phosphates from Combined Broadband Isotropic Solid-State MAS NMR Spectroscopy and DFT Calculations. *Journal of the American Chemical Society* **2012**, *134*, 17178–17185, Publisher: American Chemical Society.

(45) Middlemiss, D. S.; Ilott, A. J.; Clément, R. J.; Strobridge, F. C.; Grey, C. P. Density Functional Theory-Based Bond Pathway Decompositions of Hyperfine Shifts: Equipping Solid-State NMR to Characterize Atomic Environments in Paramagnetic Materials. *Chemistry of Materials* **2013**, *25*, 1723–1734, Publisher: American Chemical Society.

(46) Kim, J.; Middlemiss, D. S.; Chernova, N. A.; Zhu, B. Y. X.; Masquelier, C.; Grey, C. P. Linking Local Environments and Hyperfine Shifts: A Combined Experimental and Theoretical 31 P and 7 Li Solid-State NMR Study of Paramagnetic Fe(III) Phosphates. *Journal of the American Chemical Society* **2010**, *132*, 16825–16840, Publisher: American Chemical Society.

(47) Kim, J.; Ilott, A. J.; Middlemiss, D. S.; Chernova, N. A.; Pinney, N.; Morgan, D.; Grey, C. P. 2H and 27Al Solid-State NMR Study of the Local Environments in Al-Doped 2-Line Ferrihydrite, Goethite, and Lepidocrocite. *Chemistry of Materials* **2015**, *27*, 3966–3978.

(48) Kresse, G.; Hafner, J. Ab initio molecular dynamics for liquid metals. *Physical Review B* **1993**, *47*, 558–561, Publisher: American Physical Society.

(49) Kresse, G.; Hafner, J. Ab initio molecular-dynamics simulation of the liquid-metalamorphous- semiconductor transition in germanium. *Physical Review B* **1994**, *49*, 14251–14269, Publisher: American Physical Society.

(50) Kresse, G.; Furthmüller, J. Efficiency of ab-initio total energy calculations for metals and semiconductors using a plane-wave basis set. *Computational Materials Science* **1996**, *6*, 15–50, Publisher: Elsevier.

(51) Blöchl, P. E. Projector augmented-wave method. *Physical Review B* **1994**, *50*, 17953–17979, Publisher: American Physical Society.

(52) Kresse, G.; Joubert, D. From ultrasoft pseudopotentials to the projector augmented-wave method. *Physical Review B* **1999**, *59*, 1758–1775, Publisher: American Physical Society.

(53) Sun, J.; Ruzsinszky, A.; Perdew, J. Strongly Constrained and Appropriately Normed Semilocal Density Functional. *Physical Review Letters* **2015**, *115*, 036402, Publisher: American Physical Society.

(54) Sun, J.; Remsing, R. C.; Zhang, Y.; Sun, Z.; Ruzsinszky, A.; Peng, H.; Yang, Z.; Paul, A.; Waghmare, U.; Wu, X.; Klein, M. L.;

Perdew, J. P. Accurate first-principles structures and energies of diversely bonded systems from an efficient density functional. *Nature Chemistry* **2016**, *8*, 831–836, Publisher: Nature Publishing Group.

(55) Peng, H.; Yang, Z. H.; Perdew, J. P.; Sun, J. Versatile van der Waals density functional based on a meta-generalized gradient approximation. *Physical Review X* **2016**, *6*, 041005, Publisher: American Physical Society.

(56) Monkhorst, H. J.; Pack, J. D. Special points for Brillouin-zone integrations. *Physical Review B* **1976**, *13*, 5188–5192, Publisher: American Physical Society.

(57) Dovesi, R.; Orlando, R.; Civalleri, B.; Roetti, C.; Saunders, V. R.; Zicovich-Wilson, C. M. CRYSTAL: A computational tool for the ab initio study of the electronic properties of crystals. *Zeitschrift fur Kristallographie* **2005**, *220*, 571–573, Publisher: De Gruyter.

(58) Erba, A.; Desmarais, J. K.; Casassa, S.; Civalleri, B.; Donà, L.; Bush, I. J.; Searle, B.; Maschio, L.; Edith-Daga, L.; Cossard, A.; Ribaldone, C.; Ascrizzi, E.; Marana, N. L.; Flament, J.-P.; Kirtman, B. CRYSTAL23: A Program for Computational Solid State Physics and Chemistry. *Journal of Chemical Theory and Computation* **2022**, Publisher: American Chemical Society.

(59) Dovesi, R.; Erba, A.; Orlando, R.; Zicovich-Wilson, C. M.; Civalleri, B.; Maschio, L.; Rérat, M.; Casassa, S.; Baima, J.; Salustro, S.; Kirtman, B. Quantum-mechanical condensed matter simulations with CRYSTAL. *Wiley Interdisciplinary Reviews: Computational Molecular Science* **2018**, *8*, e1360, Publisher: John Wiley & Sons, Ltd (10.1111).

(60) Becke, A. D. Density-functional thermochemistry. III. The role of exact exchange. *The Journal of Chemical Physics* **1993**, *98*, 5648–5652, Publisher: American Institute of Physics.

(61) Lee, C.; Yang, W.; Parr, R. G. Development of the Colle-Salvetti correlation-energy formula into a functional of the electron density. *Physical Review B* **1988**, *37*, 785–789, Publisher: American Physical Society.

(62) Kutzelnigg, W.; Fleischer, U.; Schindler, M. *The IGLO-Method: Ab-initio Calculation and Interpretation of NMR Chemical Shifts and Magnetic Susceptibilities*; Springer, Berlin, Heidelberg, 1990; pp 165–262.

(63) Lee, J.; Seymour, I. D.; Pell, A. J.; Dutton, S. E.; Grey, C. P. A systematic study of 25 Mg NMR in paramagnetic transition metal oxides: applications to Mg-ion battery materials. *Physical Chemistry Chemical Physics* **2017**, *19*, 613–625, Publisher: The Royal Society of Chemistry.

(64) Puchala, B.; Thomas, J. C.; Natarajan, A. R.; Goiri, J. G.; Behara, S. S.; Kaufman, J. L.; Van der Ven, A. CASM — A software package for first-principles based study of multicomponent crystalline solids. *Computational Materials Science* **2023**, *217*, 111897.

(65) Yin, W.; Huang, Z.; Zhang, T.; Yang, T.; Ji, H.; Zhou, Y.; Shi, S.; Zhang, Y. P2-type layered oxide cathode with honeycomb-ordered superstructure for sodium-ion batteries. *Energy Storage Materials* **2024**, *69*, 103424.

(66) Xiao, L.; Ding, Z.; Chen, C.; Han, Z.; Wang, P.; Huang, Q.; Gao, P.; Wei, W. Insight into the Structural Disorder in Honeycomb-Ordered Sodium-Layered Oxide Cathodes. *iScience* **2020**, *23*, 100898, Publisher: Elsevier Inc.

(67) Liu, J.; Yin, L.; Wu, L.; Bai, J.; Bak, S. M.; Yu, X.; Zhu, Y.; Yang, X. Q.; Khalifah, P. G. Quantification of Honeycomb Number-Type Stacking Faults: Application to Na3Ni2BiO6 Cathodes for Na-Ion Batteries. *Inorganic Chemistry* **2016**, *55*, 8478–8492.

(68) Carlier, D.; Saadoune, I.; Ménétrier, M.; Delmas, C. Lithium Electrochemical Deintercalation fromO 2 LiCoO2 : Structure and Physical Properties. *Journal of The Electrochemical Society* **2002**, *149*, A1310, Publisher: IOP Publishing.

(69) Warren, B. E. X-Ray Diffraction in Random Layer Lattices. *Phys. Rev.* **1941**, *59*, 693–698.

(70) Seymour, I. D.; Middlemiss, D. S.; Halat, D. M.; Trease, N. M.; Pell, A. J.; Grey, C. P. Characterizing Oxygen Local Environments in Paramagnetic Battery Materials via 17O NMR and DFT Calculations. *Journal of the American Chemical Society* **2016**, *138*, 9405–9408, Publisher: American Chemical Society.

(71) Treacy, M. M. J.; Newsam, J. M.; Deem, M. W. A general recursion method for calculating diffracted intensities from crystals containing planar faults. *Proceedings of the Royal Society of London. Series A: Mathematical and Physical Sciences* **1997**, *433*, 499–520, Publisher: Royal Society.

(72) Hoang, K.; Johannes, M. Defect Physics and Chemistry in Layered Mixed Transition Metal Oxide Cathode Materials: (Ni,Co,Mn) vs (Ni,Co,Al). *Chemistry of Materials* **2016**, *28*, 1325–1334, Publisher: American Chemical Society.

(73) Bréger, J.; Meng, Y. S.; Hinuma, Y.; Kumar, S.; Kang, K.; Shao-Horn, Y.; Ceder, G.; Grey, C. P. Effect of High Voltage on the Structure and Electrochemistry of LiNi0.5Mn0.5O2: A Joint Experimental and Theoretical Study. *Chemistry of Materials* **2006**, *18*, 4768–4781, Publisher: American Chemical Society.

(74) Haworth, A. R.; Johnston, B. I. J.; Wheatcroft, L.; McKinney, S. L.; Tapia-Ruiz, N.; Booth, S. G.; Nedoma, A. J.; Cussen, S. A.; Griffin, J. M. Structural Insight into Protective Alumina Coatings for Layered Li-Ion Cathode Materials by Solid-State NMR Spectroscopy. *ACS Applied Materials & Interfaces* **2024**, *16*, 7171–7181, Publisher: American Chemical Society.

(75) Bassey, E. N.; Reeves, P. J.; Seymour, I. D.; Grey, C. P. 17O NMR Spectroscopy in Lithium-Ion Battery Cathode Materials: Challenges and Interpretation. *Journal of the American Chemical Society* **2022**, *144*, 18714–18729, Publisher: American Chemical Society.

(76) Sicklinger, J.; Metzger, M.; Beyer, H.; Pritzl, D.; Gasteiger, H. A. Ambient Storage Derived Surface Contamination of NCM811 and NCM111: Performance Implications and Mitigation Strategies. *J. Electrochem. Soc.* **2019**, *166*, A2322, Publisher: IOP Publishing.

(77) Paulsen, J. M.; Thomas, C. L.; Dahn, J. R. O2 Structure Li[sub 2/3][Ni[sub [sub 1/3]]Mn[sub [sub 2/3]]]O[sub 2]: A New Layered Cathode Material for Rechargeable Lithium Batteries. I. Electrochemical Properties. *Journal of The Electrochemical Society* **2000**, *147*, 861, Publisher: The Electrochemical Society.

(78) Van der Ven, A.; Ceder, G.; Asta, M.; Tepesch, P. First-principles theory of ionic diffusion with nondilute carriers. *Physical Review B* **2001**, *64*, 184307.

(79) Van der Ven, A.; Bhattacharya, J.; Belak, A. A. Understanding Li diffusion in Li-intercalation compounds. *Accounts of chemical research* **2013**, *46*, 1216–1225.

The data supporting this article have been included as part of the Supplementary Information.

Neutron diffraction data is available under the DOI https://doi.ill.fr/10.5291/ILL-DATA.5-23-812

We will upload the full data set to a DOI at the revisions stage, alongside crystal structures (which will be uploaded to the Inorganic Crystal Structures Database, also at revisions)